MISS LAURA BASTIANINI (Orcid ID : 0000-0003-1963-8269)
DR. MIKE ROGERSON (Orcid ID : 0000-0001-6016-0549)
DR. RAMON MERCEDES-MARTÍN (Orcid ID : 0000-0002-4410-1984)

Article type : Original Article

Corresponding author mail id: L.Bastianini@hull.ac.uk

What are the different styles of calcite precipitation within a hyperalkaline leachate? A sedimentological Anthropocene case study.

Laura Bastianini[1], Mike Rogerson[2], Ramon Mercedes-Martín[3], Timothy J. Prior[4] and William M. Mayes[1].

[1]Department of Geography, Geology and Environment, Faculty of Science and Engineering, University of Hull, Hull, United Kingdom, [2]Department of Geography and Environmental Science, Ellison Building, Northumbria University, Newcastle NE1 8ST, United Kingdom, [3]Departament de Geologia. Unitat d'Estratigrafia. Universitat Autònoma de Barcelona. Cerdanyola del Vallès E-08193, Barcelona, Spain, [4]Department of Chemistry and Biochemistry, Faculty of Science and Engineering, University of Hull, Hull, United Kingdom.

Abstract

This study aims to compare the fabrics of anthropogenic carbonates downstream of lime and steel disposal sites with models of carbonate precipitation from natural systems to elucidate potential drivers, precipitation mechanisms, morphological similarities, predictability in 3D facies distributions and depositional models of these systems. For this purpose, a combination of sedimentological, mineralogical and geochemical approaches is conducted including analysis of microfacies (petrographic microscope and electron microscopy), X-ray diffraction and hydrochemistry. The data show that both anthropogenic and natural systems exhibit clear proximal, middle and distal zones of carbonate precipitation. The main macroscopic differences are the dominance of swamp environments in the proximal zone, and the prevalence of tufa-like barrage-and-pool sequences in the middle and distal zones. Microfabrics in anthropogenic sites are

This article has been accepted for publication and undergone full peer review but has not been through the copyediting, typesetting, pagination and proofreading process, which may lead to differences between this version and the Version of Record. Please cite this article as doi: 10.1002/dep2.168

This article is protected by copyright. All rights reserved

Accepted Article

comparable to travertines but lack the sub-surface facies and at extreme pH exhibit sparry crusts without clear equivalents in travertines. This sedimentology of anthropogenic carbonates shows that calcite mineral formation is complex and not homogeneous or purely driven by thermodynamic processes. Considering the sedimentology of these human-induced systems will help us understand precipitation mechanisms which will aid both efforts to utilise anthropogenic alkaline wastes for carbon capture and manage their environmental impacts.

Keywords: anthropogenic carbonates, biotic, calcite precipitation, travertines

1. Introduction

Anthropogenic carbonates are pyrotechnological products composed of calcium carbonate, and include wood ash, lime plaster/mortar and hydraulic mortar, in addition to secondary carbonates that arise as a product of weathering a range of globally important industrial residues (Toffolo, 2020). These residues include steel slags (Roadcap et al., 2005), coal combustion residues (Dellantonio et al., 2010), chromite ore processing waste (Stewart et al., 2007), Solvay Process residues from the manufacture of soda ash (Effler et al., 2001), lime spoil (Burke et al., 2012a, b) and bauxite processing residue (Mayes et al., 2011). Many of these wastes and by-products are being produced in increasing quantities globally (Dolley, 1994), so an understanding of their broader environmental impact and characteristics, either in disposal sites or during after-use (e.g. as aggregates for road fill: (Chaurand et al., 2007)), is required to facilitate their effective management.

The leachates generated by alkaline residues are enriched in a range of metal and metalloid oxyanions which can pose serious risks to the environment, namely As, Cr, Mo, Ni, Ga and V (Burke et al., 2013; Czop et al., 2011; Mayes et al., 2011; Chaurand et al., 2007; Hobson et al., 2017). The treatment of these alkaline leachates by conventional methods (acid dosing and active aeration) is expensive, especially if it is to be continued for many decades after site closure (Evans, 2015).

The dissolution products of alkaline waste materials can raise pH values up to 12.4, well outside the pH range that will be satisfactory for any receiving waters (Mayes et al., 2008). The high pH and calcium loadings of the leachate can also cause high rates of calcium carbonate precipitation when there is contact with atmospheric CO_2, which can smother benthic communities

This article is protected by copyright. All rights reserved

(Hull et al., 2014; Koryak et al., 2002) and restrict light penetration to primary producers (Koryak et al., 2002; Roadcap et al., 2005).

Calcite precipitation within hyperalkaline sites

Precipitation of carbonates in anthropogenic sites is highly recommended as a carbon sequestration technology (Renforth et al., 2009). The formation of carbonate minerals in alkaline environments occurs when CO_2 gas is dissolved in the solution and reacts rapidly with OH^- ions (from portlandite dissolution) to form aqueous carbonate through Eq. (1).

$$Ca^{2+}_{(aq)} + 2OH^{-}_{(aq)} + CO_{2(g)} \leftrightarrow Ca^{2+}_{(aq)} + CO^{2-}_{3(aq)} + H_2O_{(l)} \leftrightarrow CaCO_{3(s)} + H_2O_{(l)} \quad (1)$$

The rate of this reaction is governed by equation 2 (Dietzel et al., 1992):

$$r = C_O \,.\, (D.k.[OH^-])^{0.5} \quad (2)$$

In this equation k is the rate constant ($cm^3.mol^{-1}.\ s^{-1}$) for hydroxylation, D is the diffusion coefficient of CO_2 through the liquid ($cm^2\ s^{-1}$) and C_o the CO_2 concentration in solution ($mol\ cm^{-3}$).

Post-industrial sites are widespread in the UK as a consequence of the country's industrial heritage and cover approximately 42,000 ha of land. Extrapolating an empirically-determined estimate that 30 kg of carbon per m^{-2} is being sequestered at these sites, Renforth et al. (2009) suggested that the United Kingdom alone stores approximately 12.7 Mt C as carbonate in brownfield soil, while Riley et al. (2020) estimate a potential carbon store of 138 Mt C in legacy slag deposits in the United Kingdom.

Riley and Mayes (2015) provide an overview of the distribution and mechanisms of calcite production in these sites. Statistical analysis of the physicochemical parameters and elemental composition of samples reveal multiple significant correlations within the streams affected by steel slag leachate. Partial Mann-Kendall (PMK) tests are also used to investigate long-term trends, in particular physical and chemical parameters that had the most complete time series at these sites (pH, alkalinity, Ca). Transient hydrological events control the use of flow as a covariate account for the fluctuations in leachate chemistry. Saturation indices (SI) of polymorphs of calcium carbonate provide a useful measure of the propensity of the hyperalkaline drainage waters to precipitate carbonate on the benthic habitats affected by the slag (Riley & Mayes, 2015).

This article is protected by copyright. All rights reserved

However, all these approaches assume that the precipitation of calcite through the system is exclusively thermodynamically controlled and is homogeneous in process. More recent research reveals evidence that the mineralization process does not conform to these assumptions. Rather, precipitation mechanisms vary within a site and can be locally controlled by kinetic processes rather than thermodynamic (Bastianini et al., 2019). Microcrystalline, sparry calcite crust forming within the water mass of a pool is unlikely to have an identical rate of formation and trace metal incorporation as "snowflake-like" dendritic carbonate crusts forming at the bottom of supercritical flows. Moreover, this study also reports microbial precipitates (clotted micrite and microbial rim carbonates) (Bastianini et al., 2019), which cannot be presumed to be controlled by the thermodynamic properties of the ambient water mass (Dupraz et al., 2009). These different crystallization processes may affect where and how quickly calcite forms, and even affect how effectively it sequesters trace elements (Saunders et al., 2014), including harmful pollutants (Burke et al., 2013; Czop et al., 2011; Mayes et al., 2011; Chaurand et al., 2007; Gomes et al., 2016, 2018; Hobson et al., 2017).Consequently, there is considerable value in investigating the sedimentology of these sites as a means to unlock a more highly resolved and process-based understanding how fast carbonate forms, where it accumulates, how long it will be preserved and how efficiently it coprecipitates contaminants. The origin of carbonate sediments can also impact their post-depositional physical properties (fine powder or lithified crusts) conditioning their use as permanent or transient earth surface carbon and environmental pollution sinks (Renforth et al., 2009).

Terrestrial carbonate sedimentology

Although the sedimentology of anthropogenic carbonates is in its infancy, significant insight can be gained by comparison with better-known tufa (ambient temperature spring, river, lake and swamp carbonate) and travertine (geothermally influenced) systems (Ford & Pedley, 1996; Capezzuoli et al., 2014; Della Porta, 2015; Pentecost, 2005). At whole-system scales for both tufa and travertine, carbonate sediment forms due to high supersaturation levels with physico-chemical precipitation (i.e. that regulated by classic thermodynamic considerations) occurring in a manner analogous to that assumed by hyperalkaline sites. The primary difference is that carbonate is generated by CO_2 degassing from excess dissolved bicarbonate (eqn. 3; Emeis et al., 1987)) as

This article is protected by copyright. All rights reserved

opposed to CO_2 in-gassing driven by excess dissolved hydroxide (eqn. 1; Clark & Fontes, 1990; Andrews et al., 1997))

$$Ca^{2+}_{(aq)} + 2HCO^{-}_{3(aq)} \leftrightarrow Ca^{2+}_{(aq)} + CO^{2-}_{3(aq)} + CO_{2(aq)} + H_2O_{(l)} \leftrightarrow CaCO_{3(s)} + CO_{2(g)} + H_2O_{(l)} (3)$$

Calcite does not precipitate directly from bicarbonate, making the pH-related conversion of $HCO^{-}_{3(aq)}$ to $CO_3^{2-}{}_{(aq)}$ a potential limit on precipitation rate (Dreybrodt et al., 1997) rather than hydroxylation of CO_2 as shown in equation 3. This is demonstrated by the observation that precipitation can be slow immediately adjacent to the spring, but rapid a few tens or hundreds of metres downstream (Dandurand et al., 1982). Precipitation rates of $CaCO_3$ from supersaturated solutions in the H_2O - CO_2 - $CaCO_3$ system are controlled by three rate-determining processes: the kinetics of precipitation at the mineral surface, mass transport of the reaction species involved to and from the mineral surface, and the slow kinetics of the overall reaction (Benning & Waychunas, 2008; Dreybrodt et al., 1997; Luttge, & Arvidson, 2010; Teng et al., 2000; White, 2020):

$$HCO^{-}_{3(aq)} + H^{+}_{(aq)} + \leftrightarrow CO_{2(aq)} + H_2O_{(l)} (4)$$

Turbulent flow and active agitation increase the area of the air–water interface and therefore promotes gas exchange (Rogerson et al., 2014). Consequently, precipitation may be enhanced at waterfalls and rapids by the same mechanism as occurs at springs (Chen et al., 2004), although physical calculations suggest this change is actually rather small (Hammer et al., 2010). The clear geomorphological evidence for enhanced carbonate precipitation at fast-flowing sites (Arenas et al., 2014) may therefore arise from processes other than gas exchange. At stagnant sites, all supply of ions to or from a growing crystal on the sediment surface is controlled by diffusion. As diffusion may be slower than precipitation, the water reacting with the crystal surface can become depleted in alkalinity, suspending the reaction. At sites with flowing water, vertical movement of ions is mostly by advection, a process that is orders of magnitude more rapid than diffusion. Flow separation occurs at the water–sediment interface forming a "diffusive boundary layer" across which ions are exchanged slowly, but these are thin if the shear velocity in the water is high (Benning & Waychunas, 2008; Liu & Dreybrodt, 1997; Luttge, & Arvidson, 2010; Teng et al., 2000; White, 2020; Zaihua et al., 1995). Consequently, alkalinity supply to the surface of a crystal growing under a rapid flow is sustained by accelerated resupply of alkalinity (Rogerson et al., 2014).

This article is protected by copyright. All rights reserved

The influence of microbial biofilms further complicates mineral formation in travertine and tufa sites, both via metabolic effects and via the influence of microbially produced extracelluar polymeric substances (EPS). The EPS monomers and polymers serve as a physical substrate for carbonate precipitation and, by extension, are passively or actively incorporated within the carbonate mineral product (Bosak & Newman, 2005; Braissant et al., 2007; Dupraz et al., 2009). This results in an array of complex processes, some of which are an active part of microbial ecological mechanisms and others are passive processes resulting from the presence of cells and EPS within sites where carbonate sediment production is already thermodynamically favoured. Following the definitions of Dupraz et al. (2009), biologically-induced mineralization involves an active if indirect action of the biota on the surrounding chemical microenvironment that results in carbonate precipitation. Biologically-influenced mineralization (the passive mineralization of an organic substrate) is a purely chemical process, but not truly abiotic as the organic matter is biologically produced. The source of alkalinity (which could be physicochemical, or metabolic) is also needed to characterise the biogenicity of a carbonate deposit (Gomes et al., 2016, 2018).

Differentiating the influences exerted by abiotic processes and biologically influenced mechanisms in the formation and early diagenesis of non-skeletal carbonates still remains problematic (Fouke, 2011; Wright, 2012; Capezzuoli et al., 2014; Brasier et al., 2015), and non-skeletal carbonates show a wide range of petrographic fabrics due to interactions between physico-chemical and biologically-influenced mechanisms (Arp et al., 2010; Mercedes-Martín et al., 2021a, 2021b). However, these studies provide great insight into what deviation from thermodynamic equilibrium processes might be expected to experience within hyperalkaline leachate sites and provide a foundation for their investigation.

Here, different styles of calcite precipitation are investigated in anthropogenic carbonates with the aim of comparing them with better-known naturally occurring systems to evidence the potential drivers, precipitation mechanisms, morphological similarities, predictability in 3D facies distributions and depositional models of these systems. This study will focus on two sites (Figure 1): Consett, a steel-slag leachate system in County Durham (United Kingdom), and Brook Bottom from Derbyshire (United Kingdom), a cement lime kiln waste environment.

2. What do we already know about anthropogenic carbonate microfacies?

An initial investigation of anthropogenic carbonate precipitate facies is reported by Bastianini et al. (2019) for the Consett site further investigated here. The findings of this study

This article is protected by copyright. All rights reserved

were summarised (Supplementary Figure S1) before building on them with further analyses of that site and additional material from Brook Bottom.

Clotted micrite

Clotted micrite is made up of a brown micritic matrix composed of fine homogeneous rounded micrite peloids (Supplementary Figure S1). Individual micrite grains reach up to 7 μm in diameter and under SEM inspection two types of calcite crystals were identified, prismatic tetrahedra *ca* 70 μm in diameter and double-terminated crystals with abundant twinned faces 100 μm in diameter. Intermingling of these heterogeneous fabrics enhance the clotted aspect recognised in thin sections. Diatoms are common components within this microfacies. These have a microbial origin, although the balance of bio-influenced and bio-induced is not known (Pedley, 1992).

Microbial Rim

This microfacies corresponds to thin black layers (180–250 μm thick) of dense micrite characterised by the presence of diverse microbial remains such as biodegraded biofilm or leaf material (Supplementary Figure S1). These have a microbial origin, probably from the breakdown of biofilms, so they are considered as being largely bio-influenced.

Carbonate dendrite

Dendrites are constituted by light-grey calcite crystals growing radially forming flower-like geometries and are made up of elongated, polycrystalline calcite giving rise to V-shaped fans that grow upon surface fronts (Supplementary Figure S1). Fans average 580 μm in length and 120 μm in width. These are only found in proximal sites which have very high mineral SI. They are associated with high rates of kinetic mineralization promoting polycrystal formation.

Calcite Shrub

Calcite shrubs are a particular subset of dendritic fabrics made up of light grey-green botryoidal crystal fans, 1–1.5 mm in height and stacked on each other as inverted cones growing on top of discontinuous horizons (Supplementary Figure S1). Botryoids are internally composed of very coarse subhedral to euhedral, elongated rhombohedral crystals forming bladed aggregates (60 μm in length) with their c-axis radiating from a previous substrate. In places, the shrubs are surrounded by diatoms and bacterial filaments. Aggregates of bladed crystals tend to develop a high intercrystalline microporosity.

This article is protected by copyright. All rights reserved

Cluster-shaped calcite

Cluster-shaped calcite appears as translucent white crystals ranging from 20 to 500 μm in length. They form a matrix made up of coarse euhedral tetrahedrons and double terminating crystals with many cluster faces, which are surrounded by a black biodegraded biofilm. The carbonates of this microfacies display extremely high intercrystalline porosity. Cluster-shaped calcite developed among bacterial filaments with an organic film forming a sticky, thin black layer around crystals which could correspond to EPS. The organic components associated with the micritic matrix of this facies along with its chemical characteristics (high alkalinity, medium pH and SI) suggest that they come from biologically influenced mineralization.

Multi-shaped calcite

The term multi-shaped calcite refers to translucent, white, delicate crystals (100–550 μm in diameter) displaying rounded external morphologies and grain-to-grain contact. These calcite crystals also exhibit trigonal, arrow and heart-shaped morphologies which seem to correspond to coarse-grained carbonate slightly reworked and stacked together. A black organic substance surrounds some crystals, which appears to be leaf material. This reworked microfacies is made up of a mixture of mineralized and organic debris.

Sparry carbonate crust

Sparry carbonate crust comprises thick sparite crusts (500–2,500 μm thick) made up of milky white to grey calcite. The partially developed crystal faces produce a very coarse, subhedral morphology. Some crystals are covered by black organic remains corresponding to degraded biofilm. Given the nature of these crystals, they develop very low intercrystalline porosity. These are diffusively grown single-crystals, associated with relatively low rates of kinetic crystallization.

Blocky calcite

Blocky calcite corresponds to single, very large crystals 500–1,500 μm in diameter, where the crystals are milky white to translucent grey. The coarse-grained euhedral crystals show distinct crystal boundaries. These appear to be a secondary phase, infilling and replacing primary fabrics and dispersed within primary materials.

3. Material and methods

3.1. Field work and data collection

Samples were collected during May 2013 along pre-established calcite saturation index (CSI) transects (Mayes et al., 2008, 2018; Riley & Mayes, 2015) within Dene Burn, Howden Burn

This article is protected by copyright. All rights reserved

and Brook Bottom (Figure 1). In these streams, calcite saturation is enhanced by alkaline discharges within the former Consett Iron Steelworks and Old Lime kiln in Brook Bottom.

The site in Consett was operational from the middle of the nineteenth century until decommissioning in the early 1980s (Figure 1). Waste up to 45 m deep, including slag, flue dusts, ashes and construction and demolition rubble were accumulated after closure in an area of 2.9 km^2 (Harber & Forth, 2001). These materials are now stored in landfill, and the leachates emerging from them are alkaline ([OH−] = 10–130 mg L^{-1}; [CO_3^{2-}] = 10–110 mg L^{-1}; [HCO_3^-] = 110 mg L^{-1}) due to meteoric waters inter-acting with the mixed industrial residue materials in the subsurface (Mayes et al., 2008, 2018; Riley & Mayes, 2015). Five carbonate samples were studied (C4, C5, DB6, DB12 and DB18) from Dene Burn (Figure 1) with a further one (C6) from Howden Burn (Figure 1). Partial results from two of these samples (C4 and C5) were reported in an earlier study (Bastianini et al., 2019).

Brook Bottom near Buxton, Derbyshire (53°14′07″N, 001°55′03″W) is a spring-fed flush, the source of which drains (and likely rises in) extensive lime kiln spoil deposits (Gunn, 1998). The Brook Bottom Springs emerge from the base of lime spoil associated with the former Harpur Hill Limeworks which operated between 1835 and 1952 (Milodowski et al., 2013). Highly alkaline leachate emerges at the Brook Bottom Springs with water pH typically in excess of pH 11.3 and dominated by Ca-OH facies (Charles et al., 2019). Four samples of secondary carbonates (BB1, BB10, BB16 and BB16) were collected at Brook Bottom from the extensive deposits in the valley floor between the source zone to the south of the site and the drainage stream to the north (Figure 1).

During sampling, on-site measurements of major physicochemical parameters (pH, electrical conductivity and water temperature) were performed using a Myron L Ultrameter® calibrated on each sample day with pH 4, 7 and 10 buffer solutions and a 1,413 μS conductivity standard, to confirm the system had not changed since previous sampling. Sample alkalinity was also obtained in the field using a two-stage titration against 1.6 N H_2SO_4 with phenolphthalein (to pH 8.3) and bromocresol green-methyl red indicators (to pH 4.6) to facilitate calculation of the constituents of sample alkalinity [i.e., hydroxyl, carbonate and bicarbonate alkalinity using the United States Geological Survey alkalinity calculator (U.S. Geological Survey, 2014)]. For each sample, three polypropylene bottles were filled, one of which was acidified with trace analysis grade concentrated HNO_3 (for total cation and trace element analysis), one of which was filtered

This article is protected by copyright. All rights reserved

(with 0.45 µm cellulose nitrate filters) prior to acidification (for dissolved cation and trace element analyses) and the other left untreated (for anion analysis).

Hydrochemistry at each of the sampling sites on the day of sampling is summarised in Tables 1 and 2, and is consistent with previous (Mayes et al., 2008) and more recent (Hull et al., 2014; Riley & Mayes, 2015; Hobson et al., 2018; Mayes et al., 2018) monitoring of these systems. Some calcium is sourced from background seepage of karst groundwater into both streams, but the majority is derived from steel slag leachate in the form of $Ca(OH)_2$. Although Ca^{2+} (aq) is elevated throughout all three streams, it is dramatically enhanced in the relatively proximal parts of Howden Burn (161–239 mg L^{-1}) and Brook Bottom (226-745 mg L^{-1}) even compared to the more proximal Dene Burn (11 to 14 mg L^{-1}). Carbon dioxide is supplied to the system from the air, and in-gasses vigorously due to the high pH of the stream waters (Eq. 1). Total alkalinity is thus high where pH is high (55–66 mg L^{-1} at Dene Burn, 264 mg L^{-1} at Howden Burn and 14 to 219 mg L^{-1} at Brook Bottom). Given this water composition, it is unsurprising that the CSI is also very high (+0.04 to +2.71), and mineral precipitation is high enough to be lethal to local microbenthos by smothering (Hull et al., 2014).

The CSI, ionic strength and Ca^{2+} and CO_3^{2-} ion activity were obtained with PHREEQC Interactive software. The kinetic calcite growth rate (R) was calculated following the formula established by Wolthers et al. (2012):

$$R = I^{-0.004}\, pH^{-10.71} r_{aq}{}^{-0.35} (S-1)^2$$

where I is the ionic strength, r_{aq} = $\{Ca^{2+}\}$ / $\{CO_3{}^{2-}\}$ activity ratio, S is the saturation ratio (Ω1/2) and R is expressed in m s^{-1}.

3.2. Mineralogy

X-ray powder diffraction (XRD) data were collected from ground samples (BB1, BB10, BB16, C4, C5, C6, DB6) mounted in stainless steel sample holders on a PANAlytical Empyrean diffractometer operating with Cu Kα1 radiation. Data were collected between $5 \leq 2\theta/^\circ \leq 80$ with a step size of 0.0262606◦ and a counting time of 304.725 s per step. Raw data were examined using the program PANAlytical HighScore (Plus) in conjunction with the PDF2 database (Gates-Rector & Blanton, 2019).

3.3. Petrographic analyses

This article is protected by copyright. All rights reserved

Optical petrography was performed with a GXM-MXP Series L3230 optical microscope at the University of Hull. Twelve thin sections were imaged with a flat-bed scanner to allow textural mapping of microfacies. Seven cuttings were carbon coated and four thin sections were imaged by Scanning Electron Microscopy (SEM) with a Zeiss EVO60 at beam currents of *ca* 40 μA and *ca* 20 kV EHT accelerating voltage (University of Hull). False colour Back-Scattered Electron images (BSE) were taken on four thin-sections to obtain high resolution compositional maps to better characterise the distribution of mineral-organic phases. An Oxford Instruments Peliter-cooled type X-Max 80 Energy Dispersive X-ray Spectroscopy (EDX) system was used to determine the abundance of specific elements in thin-sections and cuttings.

3.4. Terminology

The terminology used for petrographic descriptions follows the nomenclature of Pedley (1992), Jones et al. (2005) and Flügel (2013). The definitions of Mercedes-Martín et al. (2021) for single crystals and polycrystals are also employed in this study. A single crystal corresponds to a solid object with only one grain or crystal and hence, no grain boundaries in which an orderly three-dimensional arrangement of the atoms, ions or molecules is repeated throughout the entire volume (Jones et al., 2005). A polycrystal is an aggregate of several crystals or grains where the boundary between the grain is the grain boundary across which the orientation of the crystal changes and the point at which three boundaries meet is called the triple junction. The term "crystal shrub" was taken from Cook and Chafetz (2017) (see their figure 3C,D): "Shrubs occur in laterally continuous layers commonly 1 to 1.5 cm thick and vertically stacked shrub laminae form accumulations 10′s of centimetres in thickness. Individual laminae are composed of either a layer one shrub high or multiple shrubs stacked on top of each other. Crystal shrubs display a general overall branching outward pattern, and do not display any crystallographic influenced morphology". These arrangements differ from those recognised in carbonate dendrites, which uses the definition of Jones et al. (2005): "100–200 nm thick calcite fibres that form 3D lattice-like domains and where fibres in each dendrite have three structurally equal orientations." The terminology of Brasier et al. (2015) is used here for "sparry calcite crusts".

4. Results

4.1. Hydrochemistry

There is a significant hydrochemical gradient between the Dene Burn and Howden Burn streams and between the most proximal sites at Brook Bottom (BB1 and "tunnel" – see Figure 1A) and the most distal sites (BB10-BB16; Table 1 and 2, Figures 1 and 2). Conductivity, pH,

This article is protected by copyright. All rights reserved

alkalinity, CSI and R are dramatically more elevated in Howden Burn ([pH = 11.5]; [conductivity = 2165 µS]; [alkalinity = 264 mg.L^{-1}]; [CSI = 2.3]; [R = 4.4.10^{-10} m.s^{-1}]) than in Dene Burn ([pH = 9 – 10.7]; [conductivity = 425–450 µS]; [alkalinity = 55–66 mg L^{-1}]; [CSI = 0.04–0.96]; [R = 9.10^{-13} – 3.10^{-11}m.s^{-1}]) (Table 2). Similarly, the same parameters are considerably elevated in BB1 and "tunnel" ([pH = 12.57-12.59]; [conductivity = 8273-8290 µS]; [alkalinity = 190-219mg.L^{-1}]; [CSI = 2.65-2.71]; [R = 1.55.10^{-7}-1.87.10^{-7} m s^{-1}]) compared to BB10, BB13 and BB16 ([pH = 12.06-12.34]; [conductivity = 2374-4648 µS]; [alkalinity = 14-77mg.L^{-1}]; [CSI = 0.43-2.21]; [R = 2.4.10^{-14} -1.2.10^{-7}m.s^{-1}]).

Location C4 in Dene Burn has the lowest CSI (0.04), then followed in increasing order by locations C5 (0.25), BB16 (0.43), C2 (0.67) and C1 (0.96) (Tables 1 and 2). In Howden Burn and Brook Bottom, the values are almost doubled at the C6 (2.3), BB13 (1.96), BB10 (2.21), "tunnel" (2.65) and BB1 (2.71) sites (Tables 1 and 2) due to higher concentrations of carbonate (100–208 mg.L^{-1}) and calcium (160–745 mg.L^{-1}) (Tables 1 and 2, Figures 1 and 2).

The R is lowest at location DB18 (5.03.10^{-13}m.s^{-1}), then increases quite progressively at locations C5 (9.8.10^{-13}m.s^{-1}), DB12 (1.30.10^{-11}. s^{-1}), DB6 (3.1.10^{-11}m s^{-1}), C4 (3.4.10^{-11}m.s^{-1}) (Table 2). In Howden Burn, R is much higher (C6: R = 4.4.10^{-10}m.s^{-1}) (Table 1). In Brook Bottom, R is high in the more proximal sites BB13 (1.5.10^{-7}m.s^{-1}), BB10 (1.2.10^{-7}m.s^{-1}), "tunnel" (1.5.10^{-7}m.s^{-1}) and BB1 (1.9.10^{-7}m.s^{-1}) and is the lowest at the most distal location BB16 (2.4.10^{-14}m.s^{-1}). This places proximal Brook Bottom at even higher rates of crystal formation than those reported at Consett, meaning that although the two sites largely overlap in terms of their hydrochemistry the highest rates of mineral formation should occur only at proximal Brook Bottom and the slowest only at distal Dene Burn.

4.2. Depositional environments and carbonate microfacies

Three distinct depositional environments are observed within Consett and Brook Bottom settings, here termed the proximal, middle and distal zones. These sites all extend over 2.5 km in length, and after rising the water is affected by the local temperate climate characterised by relatively dry and high temperatures (average temperature16°C) during summer and rainy and cold winters (average temperature 4°C) (Riley & Mayes, 2015) developing typical farmland vegetation with grasses, riparian trees and groundcover. A single depositional model can be applied to all three streams, with the tripartite division based on both macro-scale geomorphology and the type and nature of carbonate sediment found within the deposits.

Proximal zone

This article is protected by copyright. All rights reserved

The proximal zone is characterised by swamp environments with soft barrages (*ca* 30 cm tall) and pools developed (locations BB1, BB10, C6, C5 and C4 on Figure 2). The water is milky, and the water is almost stagnant (flow velocity less than 1 $cm.s^{-1}$). Carbonate precipitation is so high that channels are quickly filled with fine carbonate sediment, and the water spreads and flows like a film no thicker than 10 cm. Accommodation space is quickly filled by deposits dominated by rafts of globular sparry calcite crust, clotted micrite and shrub carbonates (Figures 2 and 3; facies discussed below).

Middle zone

High precipitation rates (3.10^{-11}–$1.5.10^{-7}$ $m.s^{-1}$) allows for continued rapid crystallization of carbonate, but the style of precipitation changes to favour formation of taller barrages (*ca* 80 cm in height) at BB13 and DB6 (Figure 2). These accumulate a range of components including rafts, clotted micrite and cluster-shaped carbonates (see Figure 3 and below). The water is still milky, but the water velocity is high ($10cm.s^{-1}$ – $1m.s^{-1}$) when flowing vertically down the barrages.

Distal zone

This zone records the lowest sedimentation rates (2.10^{-14} – 1.10^{-11} $m.s^{-1}$) which occur in low relief waterfall settings. The water is clearer, and the water velocity becomes slow again overall (*ca* 1 $cm.s^{-1}$), although water moves nearly vertically on waterfall faces. The carbonate precipitation is just consuming the available accommodation space in BB16, DB12 and DB18, but pools between aggradational barrages may be several tens of centimetres deep. Close to these barrages (*ca* 50 cm in height), the energy in the system is still high depositing carbonate-coated microbial filament, clotted micrite and neomorphic sparry calcite crust microfacies (see Figure 3 and below).

4.3. Macroscopic description

All samples are light brown limestone with dark brown laminations except for the C6 sample which is light beige with beige brown laminations in a circular ring structure (Figure 4). The samples from Brook Bottom (BB1, BB10 fresh deposit, BB10 old deposit, BB13, BB16) are very friable compared to those of Consett.

4.4. Microfacies descriptions

In addition to those fabrics summarised from previous studies in Section 2, seven additional types of microfacies have been identified on the basis of fabric, mineralogy and texture (Figure 3).

Microfacies 1: Coated vegetative remains and carbonate rafts (proximal zone)

This article is protected by copyright. All rights reserved

This microfacies is made up of a poorly-sorted assemblage of flat vegetative remains coated by calcite (Figure 5A), and also carbonate rafts forming intraclastic accumulations with high interparticle porosity (Figures 3 and 5C,D). Flat organic remains correspond to fragmented and whole specimens of leaves 50 μm to 2 mm in length, and 50 μm to 200 μm in width. The external surface of these plant fragments shows multiple arcuate vault structures which are internally filled and externally coated by a cloudy, brown-coloured sparry calcite (Figure 5C,D) or even coated by globular sparry calcite crust microfacies 3 (Figure 5B). In some cases, polycrystalline calcite globular aggregates 50 to 100 μm thick can grow to form elongated structures resembling pure carbonate rafts (*sensu* Taylor & Chafetz, 2004) (Figure 5C).

Microfacies 2: Micro-peloidal and clotted micritic fabric (distal zone)

Unlike the previous study of Bastianini et al. (2019), this microfacies is composed of a highly porous and patchy micro-peloidal micritic texture of yellowish and pale brown colour (Figure 6A,B)) that can alternate with more laminated textures. Dense clotted fabrics form lumpy masses and, on some occasions protruded filamentous structures are recognised growing perpendicular to the laminae (Figure 6A,B). This microfacies host abundant inter-crystalline porosity with cavities between 10 μm and 1 mm in diameter (Figure 6A,B).

Microfacies 3: Carbonate-coated microbial filament (middle zone) This microfacies is here referred to as delicate filamentous structures (ranging from 100 to 2,500 μm in length) coated by translucent white euhedral to anhedral calcite crystals (Figure 7A). In some adjacent areas, carbonate grains are clearly detached from microbial filaments forming intraclastic accumulations (Figure 7B) already described in Consett (see Figure 7B and cluster-shaped carbonates in figure 11 from Bastianini et al., 2019).

Calcite crystals range between 5 to 30 μm in height and agglutinate around organic-rich filaments forming lumps. Coarse, euhedral tetrahedrons and double terminating crystal morphologies are recognised (Figure 7A). This microfacies displays an extremely high intercrystalline porosity with cavities fluctuating between 10 μm and 2 mm in diameter.

Microfacies 4: Globular sparry calcite crust (proximal zone)

Similar to the sparry fabrics reported by Bastianini et al. (2019), the sparry carbonate microfacies consists of globular arrangements of isopachous fans within 500 μm to 2 mm thick crusts made up of milky white to pale brown calcite (Figure 8A,B). The colour differences in the laminae might be explained by oxidation/reduction conditions changing during spar growth

This article is protected by copyright. All rights reserved

resulting in more or less Mn or Fe trapped in the calcite lattice. However, here sparry crusts nucleated upon clotted organic templates (Figure 8A,B), extending upwards and laterally. In some examples, carbonate rafts became coated with sparry carbonate crusts indicating a close relationship between microfacies (Figure 5B). Globular sparry calcite fans grew outward and laterally forming homogeneously thick bands punctuated by laminae that can be traceable between fans. Darker laminae tend to be thinner (30 μm to 90 μm in thickness) than lighter laminae (100 μm to 150 μm in thickness). Fans interfered with each other demonstrating that competitive growth took place. Most of the fans terminated in smooth curved surfaces. This microfacies displays a high intercrystalline porosity with cavities between 100 and 2,000 μm in diameter (Figure 8A,B).

Microfacies 5: Neomorphic sparry calcite crust (distal zone)

Neomorphic sparry crust consists of 500 μm –2.5 mm thick layers of milky white to grey sparry calcite crystals (Figure 9A through D). Microbial to micropeloidal and organic-rich substrates are present at the base of the sparry crust, indicating nucleation on top of them (Figure 9A). Sparry crusts are made up of isopachous fans where globular arrangements are less well defined. Indeed, EBS-SEM observations (Figure 9C,D) indicate that these crystals underwent dissolution and recrystallization leaving the interstices filled with organic-rich materials. The cracks seen in the crusts are more common at the surface and extend to different depths. The arrangement of the fissures and the overall integrity and continuity of the crusts along the samples advocates towards an authigenic origin rather than a pure intraclastic accumulation of calcite debris. For these reasons, fissures are considered to have formed by dissolution processes.

Microfacies 6: Crystal shrub fan (proximal zone)

The crystal shrub fan microfacies consist of light grey-white botryoidal crystal fans 1–3 mm in height and stacked on each other as inverted cones growing on top of discontinuous horizons (Figure 10A through D) (compare with shrub facies in Bastianini et al., 2019, their figure 10). Botryoids are internally composed of very coarse subhedral to euhedral, elongated rhombohedral crystals forming bladed aggregates (60 μm in length) (Figure 10A through D) with their c-axis radiating from a previous substrate (Figure 10A through D). Bladed crystal aggregates tend to develop incipient intercrystalline microporosity (Figure 10A through D).

In this study, analysis of a larger number of samples allows at least three generations of shrubby bands to be recognised throughout the crusts (Figure 10A,B). Every shrub generation is interrupted by a thin organic rim which is seen covering previous botryoidal terminations. Shrub

This article is protected by copyright. All rights reserved

bifurcations tend to be more developed in terminal stages where individual shrub branches show more defined limits and sometimes the presence of trapped or infiltrated organic matter (Figure 10A,B). A black degraded biofilm and some diatoms are found surrounding the crystals (Bastianini et al., 2019).

Microfacies 7: Dendrite carbonates (proximal zone)

Dendrite carbonates are light grey, tree-shaped calcite polycrystals showing multiple levels of branching (Figure 11A through D, see also Bastianini et al., 2019, their figure 9). These crystals, up to 3 cm long and 0.2 cm wide, are compact because they have only short secondary and tertiary branches (Figure 11B). Each branch consists of numerous thin (up to 0.2 mm thick), plate-like calcite crystals that are stacked "en echelon" (Figure 11A through C) (see Jones et al., 1996). The orientation of these crystals in the primary and secondary branches of the same crystal is analogous. These crystals are surrounded by a dark organic substance (Figure 11A,B).

4.5. Mineralogy

The XRD data show that all the samples are highly crystalline and correspond to pure calcite (Figures 5E, 7C, 8E and 9E) except C4, C5, C6 (corresponding to shrub, clotted micrite and dendrite mirofacies respectively) (Figures 6C, 10E and 11E) which contain a small quantity of quartz (3-5%). The EDS measurements exhibit the limited presence of Al (1.7%) and Si (1.7%) within the raft facies. Clotted micrite show the highest levels of Al (6%), Si (10,3%) and Mg (1.35%). Shrub and dendrite contain a high quantity of Si (5%), in addition to Al (0.82%) and S (1.10%).

4.6. Distribution of macrofacies and microfacies

The proximal zone in both Brook Bottom and Consett is characterised by low-gradient, swamp environments that favour the development of soft barrages and pools (Figure 12). Globular sparry calcite crust, raft, shrub and dendrite calcites constitute the microfacies diagnostic of this zone.

The middle zone corresponds to high barrages allowing the deposition of carbonate-coated microbial filaments and, less importantly, calcite rafts.

The distal zone is recognisable by its lower relief waterfall setting developing pools between aggradational barrages (Figure 12). Neomorphic sparry crust, carbonate-coated microbial filament and clotted micritic fabrics are the main deposits of this area. Both Brook Bottom and Consett face a major change in microscopic features at the limit of their proximal-distal zones but the actual microfacies are different depending on the location. In Consett, the microfacies evolve

This article is protected by copyright. All rights reserved

from principally shrub and dendrite and minor raft to reworked carbonates (carbonate-coated microbial filament and neomorphic sparry crust), whereas the microfacies at Brook Bottom evolve from raft and globular sparry calcite crust to neomorphic sparry crust.

5. Discussion

5.1. Depositional model according to macrofacies and microfacies distributions

Macrofacies distribution reveals a common depositional model between Brook Bottom and Consett, a conclusion supported by the observed macroscopic features (Figure 12). In both cases, the proximal zone is defined by pools and soft barrages, the middle zone by the largest barrages and the distal zone by smaller barrages. It is more challenging to apply a similar depositional model for both sites in microscopic terms. The proximal zone at Brook Bottom consists of rafts, a globular sparry calcite crust and, less importantly, neomorphic sparry crust whereas the Consett microfacies correspond to shrub, dendrite and carbonate-coated microbial filament. Nevertheless, both sites display intraclastic carbonate-coated microbial filaments or reworked carbonates (neomorphic sparry crusts) in the proximal zone while Consett shows minor deposition of rafts in the most proximal zone, identifiable at the macro-scale (Figure 2). The middle zone shows continued deposition of calcite rafts at Brook Bottom and altered carbonates (neomorphic sparry crust and carbonate-coated microbial filament) at Consett. Neomorphic sparry crusts at Brook Bottom and carbonate-coated microbial filaments at Consett are also characteristic of the distal zone in addition to clotted micrite.

While biofilm growth is more developed at Consett, biofilms at Brook Bottom occur only as discoloured pale and homogenous sediment crusts. The higher degree of bio-influence at Consett is confirmed by the SEM images which show more abundant diatoms at Consett, as indicated by the higher Si elemental composition (using EDX), and also the presence of quartz minerals (Goswami et al., 2012) (Figures 6, 10 and 11). This significant difference is probably due to the lethally high pH at Brook Bottom (12-12.6). Indeed, biomolecules have a range of pKa between 6.5 and 9 (Solmaz et al., 2018), significantly below 12, so at this pH biomolecules are completely dissolved and cannot construct EPS (Jones et al., 2015). Therefore, the lack of bio-influence at Brook Bottom is likely to be responsible for the dendritic and shrub fabrics only developing in Consett at a more viable pH (9).

5.2. Origin of macrofacies and microfacies

As the solution moves from the most proximal site, calcium and alkalinity are consumed, steadily reducing CSI (Figure 13). The boundary between the proximal and the distal zone (swamp

This article is protected by copyright. All rights reserved

environments to waterfalls) in both Consett and Brook Bottom does not correspond to an unusual change in CSI despite the considerable changes in macromorphology and microfacies (Figure 13). However, the proximal-distal transition is well reflected by changes in the predicted kinetic calcite growth rate (R), which shows a sudden decrease of 10^7 between samples BB1, BB10, BB13 and BB16 at Brook Bottom, and 10^3 $m.s^{-1}$ between samples C6, C4, C5 and DB6, DB12, DB18 at Consett as calcium and carbonate concentrations drop (Figure 13). In proximal Brook Bottom the very high R values promote deposition of rafts and globular sparry calcite crust (Figure 14). Howden Burn shows R values which remain high compared to other sites but are lower than proximal Brook Bottom by 10^3 $m.s^{-1}$(Table 1). Similarly, pH is much lower at Howden Burn permitting greater development of biofilm. This difference likely explains the lack of rafts but promotion of kinetically-controlled polycrystal formation at Consett. The most alkaline sites display mineralization in the surface tension layer as well as at the base. However, this requires R values at least higher than the 10^{-10} $m.s^{-1}$ found in proximal Howden Burn (Table 1). When the reaction is no longer able to sustain mineralization in the surface tension layer it switches to precipitation only at the bottom as crusts, with the turbulence of the flow also likely promoting this switch. In the absence of biofilm (as at Brook Bottom) the main fabrics are mostly globular sparry crusts constructed from mono-crystals. This is unexpected due to the very high CSI and R values at these sites. However, this fabric is likely to form as a diffusion-limited equilibrium phase. In the presence of biofilm (as at Consett), polycrystal dendrites and shrubs are formed, with the carbonate precipitation indirectly modified by a precursor organo-mineral (Dupraz et al., 2009).

Depending on the context, there are key implications arising from the observation that minerals are forming by three discrete processes in the proximal part of these systems. Formation of rafts is a direct reflection of equations 1 and 2 and arises from the nucleation of solid crystals within the surface tension layer of the water itself, likely instantaneous with hydration of the ingassing CO_2. Where water is more turbulent and precipitation less rapid downstream, nucleation occurs at the bottom of the water, below a diffuse boundary layer. In this case, the first and second step of equation 1 is no longer instantaneous and may be dependent on the advective mixing timescale of the stream rather than the reaction kinetics of equation 2. The process of carbon sequestration may also be altered by the change in control on reaction speed, with likely reduced rates of mineralization where precipitation is not occurring in the form of carbonate rafts. Where mineralization is decoupled from ingassing and occurs below a diffusive boundary layer at the

This article is protected by copyright. All rights reserved

base, this may also affect pollutant co-precipitation as availability of ions will be controlled by both advective mixing above the boundary layer and diffusion across it, rather than strictly by thermodynamic distribution of ions. Where a precipitate is bio-influenced, the rate, location and even trace element co-precipitation will also be influenced and may depart from strict thermodynamic expectations. Consequently, it is recommended that simple representations of these systems are not used outside of the small area characterised by carbonate raft precipitation at Brook Bottom. Within the middle zone, the carbonate-coated microbial filament deposited at Consett suggests a very low saturation regime and kinetic forcing (Figure 13). This microfacies correspond to bio-precipitates creating the close spatial arrangement of the calcite crystals around filamentous structures (Shiraishi et al., 2008). Furthermore, the deposition of this microfacies is characteristic of events possessing high hydraulic energy which break down the microbial filaments leaving detached crystals which are reworked to form intraclastic associations. In Brook Bottom, the middle zone corresponds to the deposition of reworked carbonates as neomorphic-sparry crust microfacies. This would imply that both carbon and pollutants sequestered in these carbonates are being transferred down the system and likely deposited in distal parts. Similarly to the proximal- distal transition, the middle- distal transition is marked by no change in CSI variance within the zones, but R values show a sudden decrease of 10^7 m.s-1 between samples BB13 and BB16 at Brook Bottom, and of 10^2 m.s-1 between samples DB6 and DB18 at Consett (Figure 13). Classic "microbialite" fabrics (micro-peloidal and clotted micritic fabric) arise under low to middle saturation regimes and occur in most locations within the distal zone of Brook Bottom and Consett (BB10, BB13, BB16, C5, C6, DB12), despite the lack of biofilm influence in proximal Brook Bottom (Figures 13 and 14). Consequently, a high proportion of distal zone precipitation suggests bio-influence and bio-induction. There is further evidence of reworking via abundant polyshaped carbonate facies. In addition, neomorphic sparry crusts occur in all sites within this zone, and EBS-SEM analysis indicate that these crystals underwent dissolution and recrystallization leaving the interstices filled by organic-rich materials. Consequently, it is hypothesised that the organic filaments are not primary precipitates. Continued reworking, combined with neomorphism and the assumed thermodynamic linkage between the water and the precipitate at these sites requires careful interpretation. The increasing dominance of microbially altered precipitation will further cause the system to deviate from thermodynamic expectations. Moreover, mass transfer downstream and / or back into solution implies that mass deposited upstream may be transferred out of the system entirely, potentially reducing the effectiveness of

This article is protected by copyright. All rights reserved

the carbonate deposit as a whole to form a stable carbon or pollutant sink. This lends support for future studies to determine whether this loss of mass is a risk to carbon sequestration or passive remediation schemes.

5.3. Comparison to natural systems

Resemblance of anthropogenic systems with natural travertine and tufa carbonates

The depositional systems described here present a stronger resemblance to travertine than tufa systems, although travertines are normally deposited from geothermally heated waters (Pentecost, 2005; Gandin & Capezzuoli, 2008). The dissolved inorganic carbon records are more elevated for travertines (>10 $mmol.L^{-1}$) than for tufa carbonates (<8 $mmol.L^{-1}$) (Pentecost, 2005; Gandin & Capezzuoli, 2008), which is consistent with the high concentrations of carbonate and bicarbonate reported in this study. Similarly, the depositional rates for anthropogenic systems (3.16 $m.year^{-1}$) are similar to travertine environments (centimetres to metres annually) but dissimilar to tufa (millimetres to centimetres annually) (Pentecost, 2005; Gandin & Capezzuoli, 2008). This study of anthropogenic systems has revealed the deposition of shrub, dendrite and globular style sparry-calcite crust and rafts, and less importantly clotted micrite micro-crystals. The first array of carbonate styles is similar to the range of crystal types present in travertine systems (where dendritic, bladed, or spherulitic precipitates are common) whereas micritic to micro-sparitic crystals are more common in tufa environments (Pentecost, 2005; Gandin & Capezzuoli, 2008).

Here, anthropogenic carbonate sedimentary systems are compared to the travertine models of Capezzuoli et al. (2014) to further investigate the similarity between these well-studied systems and the relatively limited information available for anthropogenic settings (Figure 12). Like anthropogenic systems, travertines are also divided into three different environments: vent environment (proximal), slope environment (middle) and distal environment, facilitating comparisons among them.

Macroscopic features

In proximal environments, travertines accumulate around discrete springs associated with convective hydrothermal systems (Capezzuoli et al., 2014; Fouke, 2001) (Figure 12). Depending on the chemical and physical characteristics of these thermal waters, irregular masses of filamentous bacteria may locally colonise pool and channel margins in the vicinity of the vent (Capezzuoli et al., 2014) (Figure 12). The resulting macro-morphologies are represented by

This article is protected by copyright. All rights reserved

circular mounds and linear-to-arcuate fissure ridges (Capezzuoli et al., 2014) (Figure 12). Travertine fissure ridges mainly develop on brittle-fracturing bedrock exposed at the surface, while isolated thermal springs, such as towers, pinnacles and mounds, generally form on unconsolidated sediments (Hancock et al., 1999; Brogi & Capezzuoli, 2009). At the water surface, travertine might form rapidly and quickly develops into steep-sided constructional morphologies as a result of the nucleation of solid crystals within the surface tension layer. Anthropogenic carbonates also occur within pools and barrages comparable to the steep-sided constructional morphologies and mounds (Figure 12), but the swampy raft and polycrystal-rich proximal zone of anthropogenic carbonates are quite unlike the hard proximal deposits of travertines, with their characteristic positive relief. Comparison is straightforward in the middle zone, where terraces (gently inclined slope deposits) and terrace fronts (steep slopes around graben fault margins) (Altunel & Hancock, 1993b) closely resemble the elevated barrages present in the middle zone of anthropogenic carbonates (Figure 12). The distal zone of travertines is typically of low relief with the development of marshes (Guo & Riding, 1998), shallow lakes (Sant'Anna et al., 2004) or alluvial plains (Brogi et al., 2012). They are specifically transitional environments where travertine fabrics grade imperceptibly into tufa fabrics and biotic controls on depositional processes progressively increase (Rainey & Jones, 2009). The same gradational transition is found in the distal zone of anthropogenic carbonates, which exhibit low relief within waterfall settings and where the developing impounded pools and the biomass biofilm significantly influence carbonate precipitation (Figure 12).

Microscopic features

Travertines also exhibit carbonate raft microfacies formation at proximal sites reflecting similar coupling of mineral precipitation at the air-water interface as gas exchange, although the gas is exsolving, as in equation 3, rather than dissolving, as in equation 1, and the rate is governed by the dissociation of bicarbonate (Dreybrodt et al., 1997) not equation 2 (Figure 12). Large domes forming around vent resurgence points are characterised by a vast array of crystal forms, from coarse dendritic to platy and spherulitic calcite (Jones & Renaut, 1996, 1998, 2010) (Figure 12). Shallow pools in the vicinity of the vent are often associated with micritic to microsparitic laminae which may build up into small (millimetre to centimetre scale) shrubby growths (Capezzuoli et al., 2014) (Figure 12). Shrubs are also deposited in the proximal zone of anthropogenic carbonates within shallow pools (Figure 12). Chafetz et al. (2018) also report a biogenic influence on the formation of shrubby carbonates. The shallow plumbing of geothermal

This article is protected by copyright. All rights reserved

systems, representing conduits for the upwelling of thermal water, is lined by variably shaped calcite/aragonite crystals (sparitic, acicular, dendritic and platy) developed into non-porous, sub-vertical crystalline laminated crusts (banded travertine: Altunel & Hancock, 1993a,b, 1996; Della Porta, 2015; Gandin & Capezzuoli, 2014; Uysal et al., 2007, 2009, 2011), but these are not comparable in origin to the crusts forming below open water in the anthropogenic systems (Figure 12). The lack of these crusts in travertines may reflect the ubiquitous biofilms, making them more comparable to Consett. In the middle zone, travertines display a diverse range of lithofacies (crystalline crust, shrubs, coated bubbles and paper-thin rafts) (Figure 12). Similarly, rafts are also deposited in the middle zone environment in this study. In the distal zone, travertine deposits are often dominated by lithoclastic material (hillwash breccia), but coated grains, in situ coated macrophyte stems and subordinate, massive bedded layers of clotted peloidal micrite may develop (Capezzuoli et al., 2014) (Figure 12). This compares well with anthropogenic systems, in which distal sites are characterised by the formation of clotted micrite and reworked/altered material such as carbonate-coated microbial filament and neomorphic sparry crust (Figure 12).

Differences between travertine and anthropogenic systems

At the macro-scale, travertines present a more diverse range of environments represented by thermal springs, pools, channels, towers, pinnacles and mounds (Capezzuoli et al., 2014), whereas anthropogenic systems only present pools and low-angle terraced slopes. However, comparatively more research has been performed in natural settings and greater diversity of microfacies can be found in anthropogenic systems. Regardless, the proximal zone within anthropogenic systems is distinctly different from travertine environments. The middle zones are more comparable, but terraces and range-front sheets (Capezzuoli et al., 2014) are not geomorphologically identical to the elevated barrages of anthropogenic systems, which share morphological and possibly microfacies similarities with tufa phytoherm constructions (Pedley, 1992). The travertine middle zone provides evidence of a wide range of microfacies (crystalline crust, shrub, coated bubbles and raft) (Capezzuoli et al., 2014), while anthropogenic microfacies are considerably more limited (raft and reworked carbonates). As with the overall diversity of systems, this may simply reflect less work carried out in anthropogenic systems. The distal zones are highly similar, despite the continued presence of barrage-like waterfall settings in anthropogenic systems unlikely the alluvial plain and shallow lakes for travertines (Capezzuoli et al., 2014).

6. Conclusion

This article is protected by copyright. All rights reserved

Anthropogenic systems show specific sedimentologies which can be partially comparable to those from travertine natural systems although requiring their own depositional models. Like travertines, anthropogenic sites develop in a tripartite division including proximal, middle and distal zones forming partially analogous geomorphologies. The major geomorphological differences are the dominance of swamp environments in the proximal zone, and the prevalence of tufa-like barrage-and-pool sequences in the middle and distal zones. Microfabrics in anthropogenic sites are similar to those from travertine environments but lack the sub-surface facies and, at extreme pH, exhibit a globular sparry crust without a clear equivalent in travertines. An initial depositional model is proposed here for anthropogenic sites as a means of stimulating further international research into these important geosystems.

This sedimentological model of anthropogenic carbonates shows that the formation of calcite minerals is complex and not homogeneous or purely driven by thermodynamic processes. Precipitation within the surface tension layer is reported here, which is likely to be directly controlled by the rate of CO_2 dissolution, but precipitation also occurs below the diffusive boundary layer and this may be influenced by advective transport in the water column. In addition, both diffusively limited and kinetically limited crystal forms are found, indicating differences in crystal assembly style which may alter trace element incorporation and co-precipitation rates. Interestingly, bio-influenced and bio-induced fabrics were identified suggesting that the site, rate, style and trace element incorporation into precipitates can be altered by the presence of microbial biofilms. Anthropogenic systems are as complex as naturally occurring tufa and travertine, and equally approachable to standard sedimentological analysis.

Proper understanding of the sedimentology of these systems will improve our ability to predict and manage the carbon sequestration and pollutant removal which are unique features of this type of continental carbonate system. Without this knowledge, researchers will be challenged to predict the rates and locations of precipitation and to compare bulk sediment composition to water composition assuming they are driven by thermodynamic equilibrium. Finally, a better understanding of the extent of the reworking processes and the nature of neomorphism and recrystallization is needed to accurately predict the stability of the carbon and pollutant sinks during the temporal and spatial evolution of these systems after deposition.

ACKNOWLEDGEMENTS

MR would like to thank Brian Jones for encouragement to study the sedimentology of these sites and apologises for his tardiness in getting started. We would like to thank Mark Anderson for the

This article is protected by copyright. All rights reserved

Accepted Article

production of thin sections. LB is supported by a funded doctoral studentship from the University of Hull. This manuscript greatly benefited from the remarks of two anonymous reviewers.

CONFLICT OF INTEREST

The authors declare that they have no known competing financial interests or personal relationships that could have appeared to influence the work reported in this paper.

AUTHOR CONTRIBUTIONS

The idea for this manuscript arose from the discussion between all authors. LB executed the petrographic analysis and drafted the manuscript. MR made improvements through the whole manuscript. RM-M provided insight on the facies descriptions and the discussion. TP collected and interpreted X-ray diffraction data. WM contributed to the hydrochemical data and their interpretation.

Table 1: Hydrochemistry dataset of the Brook Bottom samples including pH, temperature, major ion concentrations, total alkalinity, calcite saturation index, ionic strength, activity and calcite growth rate.

Table 2: Hydrochemistry dataset of the Consett samples including pH, temperature, major ion concentrations, total alkalinity, calcite saturation index, ionic strength, activity and calcite growth rates from the research works of Mayes et al. (2008, 2018), Hull et al. (2014), Riley and Mayes (2015), Hobson et al. (2018)

FIGURE CAPTIONS

Figure 1: (A) Location map of the Brook Bottom (BB) samples (BB1, BB13, BB10 fresh, BB10 old deposit, BB16) where the yellow part represents the carbonate deposit. (B) Topographic map with the Brook Bottom samples (BB1, BB13, BB10 fresh, BB10 old deposit, BB16) after Ordnance Survey map. (C) Location map of the Consett (C) freshwater samples in Howden Burn (C6) and Dene Burn (DB) (C4, C5, DB6, DB12, DB18) after Historic OS maps. (D) Topographic map with the Consett freshwater samples in Howden Burn (C6) and Dene Burn (C4, C5, DB6, DB12, DB18) after Ordnance Survey map.

Figure 2: Environmental pictures of the downstream transects of Howden Burn, Dene Burn and Brook Bottom with the localisation of the riffle, waterfall, and woodland.

Figure 3: (A) Original thin sections from the Brook Bottom (BB) (BB1, BB13, BB10 fresh, BB10 old deposit, BB16) and Consett (C) freshwater samples in Howden Burn (C6) and Dene Burn

This article is protected by copyright. All rights reserved

(DB) (C4, C5, DB6, DB12, DB18) with the locations of the optical microscope images. The locations are respectively designated by the number of the figure from this manuscript followed by the letter corresponding to the subsection in the figure. (B) Interpreted thin-sections with the colours representing the different microfacies. The locations of the optical microscope images are respectively designated by the number of the figure from this manuscript followed by the letter corresponding to the subsection in the figure.

Figure 4 Macroscopic images of the Brook Bottom (BB) (BB1, BB13, BB10 fresh, BB10 old deposit, BB16) and Consett (C) freshwater samples in Howden Burn (C6) and Dene Burn (DB) (C4, C5, DB6, DB12, DB18).

Figure 5: Coated vegetative remains and carbonate raft (microfacies 1). (A) Assemblage of brown coloured, flat and elongated vegetative remains (arrow) coated by calcite thin films. (B) Some flat remains (arrow) are covered in globular sparry calcite crusts (Gs); interparticle porosity (p) is very abundant. (C) SEM photomicrograph of carbonate rafts (R) covered by multiple arcuate vault structures (Vs) consisting of cloudy, brown-coloured sparry calcite. (D) BSE-SEM image of poorly sorted carbonate rafts covered by vault structures (VS). Some polycrystalline calcite globular aggregates (pcg) can grow laterally to form elongated structures. (E and F) XRD pattern and EDX spot analysis, respectively, indicating a calcite mineralogy.

Figure 6: Micro-peloidal and clotted micritic (microfacies 2). (A and B) Patchy micropeloidal micritic textures (pel) alternate with laminated textures (arrows). Filamentous clotted structures can be seen perpendicular to laminae (fil-pel). In some cases, lumpy micropeloidal masses (lum-pel) develop in association with laminated textures. Abundant inter-crystalline porosity (p) is observed in this microfacies.(C and D) SEM images of the microfacies clotted micrite. XRD pattern and EDX spot analysis, respectively, indicating that calcite and quartz are present.

Figure 7: Carbonate-coated microbial filament (microfacies 3). (A) Double terminating calcite crystal morphologies agglutinated around organic-rich filamentous structures (arrows) forming crystal lumps. High intercrystalline porosity (p) is recognised between filaments. (B) Double terminating calcite crystals can be detached from microbial filaments forming intraclastic

This article is protected by copyright. All rights reserved

accumulations embedded in organic-rich matrices (o). (C and D) XRD pattern and EDX spot analysis, respectively, indicating that calcite is the predominant mineralogy.

Figure 8: Globular sparry calcite crust (microfacies 4). (A and B) Thick isopachous calcite fans with globular arrangements (Gs) growing on top of clotted peloidal templates (arrows). Fans consist of thin darker laminae and thick lighter laminae extending laterally. Competitive growth defines sharp boundaries between fans (cg). This microfacies displays a high intercrystalline porosity (p). (C) SEM image showing the external smooth curved surfaces of the fans (Gs). (D) BSE-SEM image displaying sparry crusts growing on top of organic substrates (arrows). Note thin concentric, darker laminae within fans. (E and F) XRD pattern and EDX spot analysis, respectively, indicating that calcite is the predominant mineralogy.

Figure 9: Neomorphic sparry crust (microfacies 5). *(*A and B) Neomorphic sparry crusts growing on top of organic-rich substrates (arrows). Corroded areas (cor) through irregular surfaces on the external part of the crusts are common. (C and D) BSE-SEM images showing cracking of the crusts where fissures (cr) reach different depths showing no apparent reworking. (E and F) XRD pattern and EDX spot analysis, respectively, indicating that calcite is the predominant mineralogy.

Figure 10: Crystal shrub (microfacies 6). *(*A and B) Light grey-white botryoidal crystal fans 1–3 mm in height and stacked on each other as inverted cones growing on top of discontinuous horizons (arrows). (C and D) BSE-SEM images showing bladed crystal aggregates developing incipient intercrystalline microporosity (arrows). (E and F) XRD pattern and EDX spot analysis, respectively, indicating that calcite and quartz are present.

Figure 11: Dendrite carbonates (microfacies 7). *(*A and B) Light grey calcite polycrystals showing multiple levels of branching (arrows). (C and D) BSE-SEM images showing that each branch consists of numerous thin (up to 0.2 mm thick), plate-like calcite crystals that are stacked en echelon (arrows). (E and -F) XRD pattern and EDX spot analysis, respectively, indicating that calcite and quartz are present.

Figure 12: Comparative depositional model between anthropogenic carbonate and travertine systems after Capezuolli et al. (2014) and Mancini et al. (2019).

Figure 13: Charts showing the pH, temperature and Calcite Saturation Index (CSI), and the major ions and total carbonate alkalinity for the Brook Bottom and Consett samples.

This article is protected by copyright. All rights reserved

Figure 14: (A) Diagram showing the Calcite Saturation Index (CSI), pH, calcite growth rate (R) versus distribution of microfacies according to the sample locations at Brook Bottom (BB) BB1, BB13, BB10 fresh, BB10 old deposit, BB16 and Consett (C) freshwater samples in Howden Burn (C6) and Dene Burn (DB) (C4, C5, DB6, DB12, DB18). (B) Depositional model summarising the lateral changes of the dominant microfacies: Coated vegetative remains and carbonate raft (R), Micro-peloidal and clotted micritic (CM), Carbonate-coated microbial filament (C), Globular sparry calcite crust (G), Neomorphic sparry crust (N), Crystal shrub (CS) and Dendrite (D).

SUPPLEMENTARY FIGURES

Figure S1: Previous fabrics after Bastianini et al. (2019). (A) Clotted micrite (B) Microbial rim (C) Carbonate Dendrite (D) Calcite shrub (E) Cluster-shaped calcite (F) Multi-shaped carbonate (G) Sparry carbonate crust (H) Blocky calcite.

REFERENCES

Altunel, E. R. H. A. N., & Hancock, P. L. (1993). Morphology and structural setting of Quaternary travertines at Pamukkale, Turkey. Geological Journal, 28(3-4), 335-346.

Altunel, E., & Hancock, P. L. (1996). Structural attributes of travertine-filled extensional fissures in the Pamukkale Plateau, Western Turkey. International Geology Review, 38(8), 768-777.

Andrews, J. E., Riding, R., & Dennis, P. F. (1997). The stable isotope record of environmental and climatic signals in modern terrestrial microbial carbonates from Europe. Palaeogeography, Palaeoclimatology, Palaeoecology, 129(1-2), 171-189.

Arenas, C., Vázquez-Urbez, M., Pardo, G., & Sancho, C. (2014). Sedimentology and depositional architecture of tufas deposited in stepped fluvial systems of changing slope: lessons from the Quaternary Añamaza valley (Iberian Range, Spain). Sedimentology, 61(1), 133-171.

Arp, G., Bissett, A., Brinkmann, N., Cousin, S., de Beer, D., Friedl, T., Mohr, KI., Neu,.TR., Reimer, A., Shiraishi, F., Stackebrandt, E., Zippel, B. (2010). Tufa-forming biofilms of German karstwater streams: microorganisms, exopolymers, hydrochemistry and calcification. In: Pedley M, Rogerson M (eds) Tufas and Speleothems. Geological Society of London Special Publication 336: 83–118.

This article is protected by copyright. All rights reserved

Bastianini, L., Rogerson, M., Mercedes-Martín, R., Prior, T. J., Cesar, E. A., & Mayes, W. M. (2019). What causes carbonates to form "shrubby" morphologies? An Anthropocene limestone case study. Frontiers in Earth Science, 7, 236.

Benning, L. G., & Waychunas, G. A. (2008). Nucleation, growth, and aggregation of mineral phases: Mechanisms and kinetic controls. In Kinetics of Water-Rock Interaction (pp. 259-333). Springer, New York, NY.Bosak, T., & Newman, D. K. (2005). Microbial kinetic controls on calcite morphology in supersaturated solutions. Journal of Sedimentary Research, 75(2), 190-199.

Braissant, O., Cailleau, G., Duprez, C. and Verrecchia, E.P. (2003) Bacterially induced mineralization of calcium carbonate in terrestrial environments: the role of exopolysaccharides and amino acids. J. Sed. Res., 73, 485–490.

Braissant, O., Decho, A. W., Dupraz, C., Glunk, C., Przekop, K. M., & Visscher, P. T. (2007). Exopolymeric substances of sulfate-reducing bacteria: interactions with calcium at alkaline pH and implication for formation of carbonate minerals. Geobiology, 5(4), 401-411.

Brasier, A. T., Rogerson, M. R., Mercedes-Martin, R., Vonhof, H. B., & Reijmer, J. J. G. (2015). A test of the biogenicity criteria established for microfossils and stromatolites on Quaternary tufa and speleothem materials formed in the "Twilight Zone" at Caerwys, United Kingdom. Astrobiology, 15(10), 883-900.

Brogi, A., & Capezzuoli, E. (2009). Travertine deposition and faulting: the fault-related travertine fissure-ridge at Terme S. Giovanni, Rapolano Terme (Italy). International Journal of Earth Sciences, 98(4), 931-947.

Brogi, A., Capezzuoli, E., Buracchi, E., & Branca, M. (2012). Tectonic control on travertine and calcareous tufa deposition in a low-temperature geothermal system (Sarteano, Central Italy). Journal of the Geological Society, 169(4), 461-476.

Burke, I. T., Mortimer, R. J., Palaniyandi, S., Whittleston, R. A., Lockwood, C. L., Ashley, D. J., & Stewart, D. I. (2012). Biogeochemical reduction processes in a hyper-alkaline leachate affected soil profile. Geomicrobiology Journal, 29(9), 769-779.

Burke, I. T., Peacock, C. L., Lockwood, C. L., Stewart, D. I., Mortimer, R. J., Ward, M. B., ... & Mayes, W. M. (2013). Behavior of aluminum, arsenic, and vanadium during the neutralization of red mud leachate by HCl, gypsum, or seawater. Environmental science & technology, 47(12), 6527-6535.

Capezzuoli, E., Gandin, A., & Pedley, M. (2014). Decoding tufa and travertine (fresh water carbonates) in the sedimentary record: the state of the art. Sedimentology, 61(1), 1-21.

This article is protected by copyright. All rights reserved

Chafetz, H. S., & Folk, R. L. (1984). Travertines; depositional morphology and the bacterially constructed constituents. Journal of Sedimentary Research, 54(1), 289-316.

Chafetz, H., Barth, J., Cook, M., Guo, X., & Zhou, J. (2018). Origins of carbonate spherulites: implications for Brazilian Aptian pre-salt reservoir. Sedimentary Geology, 365, 21-33.

Chaurand, P., Rose, J., Briois, V., Olivi, L., Hazemann, J. L., Proux, O., ... & Bottero, J. Y. (2007). Environmental impacts of steel slag reused in road construction: A crystallographic and molecular (XANES) approach. Journal of Hazardous Materials, 139(3), 537-542.

Charles, C. J., Rout, S. P., Wormald, R., Laws, A. P., Jackson, B. R., Boxall, S. A., & Humphreys, P. N. (2019). In-situ biofilm formation in hyper alkaline environments. Geomicrobiology Journal, 36(5), 405-411.

Chen, Z., Grasby, S. E., & Osadetz, K. G. (2004). Relation between climate variability and groundwater levels in the upper carbonate aquifer, southern Manitoba, Canada. Journal of Hydrology, 290(1-2), 43-62.

Clark, I. D., & Fontes, J. C. (1990). Paleoclimatic reconstruction in northern Oman based on carbonates from hyperalkaline groundwaters. Quaternary Research, 33(3), 320-336.

Czop, E., Economou, A., & Bobrowski, A. (2011). A study of in situ plated tin-film electrodes for the determination of trace metals by means of square-wave anodic stripping voltammetry. Electrochimica acta, 56(5), 2206-2212.

Dandurand, J. L., Gout, R., Hoefs, J., Menschel, G., Schott, J., & Usdowski, E. (1982). Kinetically controlled variations of major components and carbon and oxygen isotopes in a calcite-precipitating spring. Chemical geology, 36(3-4), 299-315.

Della Porta, G. (2015). Carbonate build-ups in lacustrine, hydrothermal and fluvial settings: comparing depositional geometry, fabric types and geochemical signature. Geological Society, London, Special Publications, 418(1), 17-68.

Dellantonio, A., Fitz, W. J., Repmann, F., & Wenzel, W. W. (2010). Disposal of coal combustion residues in terrestrial systems: contamination and risk management. Journal of environmental quality, 39(3), 761-775.

Dietzel, M., Usdowski, E., & Hoefs, J. (1992). Chemical and 13C/12C-and 18O/16O-isotope evolution of alkaline drainage waters and the precipitation of calcite. Applied Geochemistry, 7(2), 177-184.

Dolley, T. P. (1994). The Mineral Industry of Morocco and Western Sahara. USGS Mineral Yearbook.

This article is protected by copyright. All rights reserved

Dreybrodt, W., Eisenlohr, L., Madry, B., & Ringer, S. (1997). Precipitation kinetics of calcite in the system CaCO3 ? H2O ? C02: The conversion to CO2 by the slow process H^++ $HCO3^- \rightarrow CO_2$+ H_2O as a rate limiting step. Geochimica et Cosmochimica Acta, 61(18), 3897-3904.

Dupraz, C., Reid, R. P., Braissant, O., Decho, A. W., Norman, R. S., and Visscher, P. T. (2009). Processes of carbonate precipitation in modern microbial mats. Earth Sci. Rev. 96, 141–162. doi: 10.1016/j.earscirev.2008.10.005

Effler, S. W., Brooks, C. M. M., & Driscoll, C. T. (2001). Changes in deposition of phytoplankton constituents in a Ca2+ polluted lake. Environmental science & technology, 35(15), 3082-3088.

Emeis, K. C., Richnow, H. H., & Kempe, S. (1987). Travertine formation in Plitvice National Park, Yugoslavia: chemical versus biological control. Sedimentology, 34(4), 595-609.

Evans K (2015): Successes and challenges in the management and use of bauxite residue. In: Pontikes Y (Hrsg.), Bauxite residue valorisation and best practices, Leuven, Belgium, pp. 53–60

Fernandez-Diaz, L., Putnis, A., Prieto, M., & Putnis, C. V. (1996). The role of magnesium in the crystallization of calcite and aragonite in a porous medium. Journal of Sedimentary Research, 66(3), 482-491.

Fjellheim A. & Raddum G.G. (1995) Benthic animal response after liming of three South Norwegian rivers. Water, Air and Soil Pollution, 85, 931-936.

Flügel, E. (2013). Microfacies of Carbonate Rocks: Analysis, Interpretation and Application. Berlin: Springer Science and Business Media.

Ford, T. D., & Pedley, H. M. (1996). A review of tufa and travertine deposits of the world. Earth-Science Reviews, 41(3-4), 117-175.

Fouke, B. W. (2001). Depositional facies and aqueous-solid geochemistry of travertine-depositing hot springs (angel terrace, mammoth hot springs, yellowstone national park, USA): reply. Journal of sedimentary research, 71(3), 497-500.

Fouke, B. W. (2011). Hot-spring Systems Geobiology: abiotic and biotic influences on travertine formation at Mammoth Hot Springs, Yellowstone National Park, USA. Sedimentology, 58(1), 170-219.

This article is protected by copyright. All rights reserved

Gandin, A., & Capezzuoli, E. (2008). Travertine versus calcareous tufa: Distinctive petrologic features and stable isotopes signatures. Italian Journal of Quaternary Sciences, 21(1B), 125-136.

Gandin, A., & Capezzuoli, E. (2014). Travertine: distinctive depositional fabrics of carbonates from thermal spring systems. Sedimentology, 61(1), 264-290.

Gates-Rector, S., & Blanton, T. (2019). The powder diffraction file: a quality materials characterization database. Powder Diffraction, 34(4), 352-360.

Gomes, H. I., Jones, A., Rogerson, M., Burke, I. T., & Mayes, W. M. (2016). Vanadium removal and recovery from bauxite residue leachates by ion exchange. Environmental Science and Pollution Research, 23(22), 23034-23042.

Gomes, H. I., Mayes, W. M., Baxter, H. A., Jarvis, A. P., Burke, I. T., Stewart, D. I., & Rogerson, M. (2018). Options for managing alkaline steel slag leachate: A life cycle assessment. Journal of Cleaner Production, 202, 401-412.

Goswami, B., Choudhury, A., & Buragohain, A. K. (2012). Luminescence properties of a nanoporous freshwater diatom. Luminescence, 27(1), 16-19.

Grassmann, O., Neder, R.B., Putnis, A. and Lobmann, P. (2003) Biomimetic control of crystal assembly by growth in an organic hydrogel network. Am. Mineral., 88, 647–652.

Guo, L. I., & Riding, R. (1998). Hot-spring travertine facies and sequences, Late Pleistocene, Rapolano Terme, Italy. Sedimentology, 45(1), 163-180.

Hammer, Ø., Dysthe, D. K., & Jamtveit, B. (2007). The dynamics of travertine dams. Earth and Planetary Science Letters, 256(1-2), 258-263.

Hammer, Ø. (2008). Watch your step. Nature Physics, 4(4), 265-266.

Hammer, Ø., Dysthe, D. K., Lelu, B., Lund, H., Meakin, P., & Jamtveit, B. (2008). Calcite precipitation instability under laminar, open-channel flow. Geochimica et Cosmochimica Acta, 72(20), 5009-5021.

Hammer, Ø., Dysthe, D. K., & Jamtveit, B. (2010). Travertine terracing: patterns and mechanisms. Geological Society, London, Special Publications, 336(1), 345-355.Hancock, P. L., Chalmers, R. M. L., Altunel, E. R. H. A. N., & Çakir, Z. (1999). Travitonics: using travertines in active fault studies. Journal of Structural Geology, 21(8-9), 903-916.

Harber, A. J., & Forth, R. A. (2001). The contamination of former iron and steel works sites. Environmental Geology, 40(3), 324-330.

This article is protected by copyright. All rights reserved

Hobson, A. J., Stewart, D. I., Bray, A. W., Mortimer, R. J., Mayes, W. M., Rogerson, M., & Burke, I. T. (2017). Mechanism of vanadium leaching during surface weathering of basic oxygen furnace steel slag blocks: a microfocus X-ray absorption spectroscopy and electron microscopy study. Environmental science & technology, 51(14), 7823-7830.

Hobson, A. J., Stewart, D. I., Bray, A. W., Mortimer, R. J., Mayes, W. M., Riley, A. L., ... & Burke, I. T. (2018). Behaviour and fate of vanadium during the aerobic neutralisation of hyperalkaline slag leachate. Science of the total environment, 643, 1191-1199.

Hull, S. L., Oty, U. V., & Mayes, W. M. (2014). Rapid recovery of benthic invertebrates downstream of hyperalkaline steel slag discharges. Hydrobiologia, 736(1), 83-97.

Jones, B. and Renaut, R.W. (1996) Skeletal crystals of calcite and trona from hot-spring deposits in Kenya and New Zealand. J. Sed. Res., 66, 265–274.

Jones, B. and Renaut, R.W. (1998) Origin of platy calcite crystals in hot-spring deposits in the Kenya rift valley. J. Sed. Res., 68, 913–927.

Jones, B., Renaut, R. W., Bernhart Owen, R., & Torfason, H. (2005). Growth patterns and implications of complex dendrites in calcite travertines from Lýsuhóll, Snæfellsnes, Iceland. Sedimentology, 52(6), 1277-1301.

Jones, B. and Renaut, R.W. (2010) Calcareous spring deposits in continental settings. In: Developments in Sedimentology: Carbonates in Continental Settings: Facies, Environments and Processes (Eds A.M. Alonso-Zarza and L.H. Tanner), pp. 177–224. Elsevier, Amsterdam.

Jones, E. M., Cochrane, C. A., & Percival, S. L. (2015). The effect of pH on the extracellular matrix and biofilms. Advances in wound care, 4(7), 431-439.

Koryak, M., Stafford, L. J., Reilly, R. J., & Magnuson, M. P. (2002). Impacts of steel mill slag leachate on the water quality of a small Pennsylvania stream. Journal of Freshwater Ecology, 17(3), 461-465.

Liu, Z.H., Dreybrodt, W., 1997. Dissolution kinetics of calcium carbonate minerals in H_2O–CO_2 solutions in turbulent flow. The role of the diffusion boundary layer and the slow reaction $H_2O+CO_2=H^+ + HCO_3^-$. Geochimica et Cosmochimica Acta 61, 2879–2889Luttge, A., & Arvidson, R. S. (2010). Reactions at surfaces: A new approach integrating interferometry and kinetic simulations. Journal of the American Ceramic Society, 93(11), 3519-3530.

Mancini, A., Capezzuoli, E., Erthal, M., Swennen, R., 2019. Hierarchical approach to define travertine depositional systems: 3D conceptual morphological model and possible

This article is protected by copyright. All rights reserved

applications. Mar. Pet. Geol. 103, 549–563.Mayes, W. M., Younger, P. L., and Aumônier, J. (2008). Hydrogeochemistry of alkaline steel slag leachates in the UK. Water Air Soil Pollut. 195, 35–50. doi: 10.1007/s11270-008-9725-9

Mayes, W. M., Jarvis, A. P., Burke, I. T., Walton, M., Feigl, V., Klebercz, O., & Gruiz, K. (2011). Dispersal and attenuation of trace contaminants downstream of the Ajka bauxite residue (red mud) depository failure, Hungary. Environmental science & technology, 45(12), 5147-5155.

Mayes, W. M., Riley, A. L., Gomes, H. I., Brabham, P., Hamlyn, J., Pullin, H., et al. (2018). Atmospheric CO_2 sequestration in iron and steel slag: consett, county Durham, United Kingdom. Environ. Sci. Technol. 52, 7892–7900. doi: 10.1021/acs.est.8b01883

Meldrum, F. C., and Cölfen, H. (2008). Controlling mineral morphologies and structures in biological and synthetic systems. Chem. Rev. 108, 4332–4432.

doi: 10.1021/cr8002856Mercedes-Martín, R., Rao, A., Rogerson, M., & Sánchez-Román, M. (2021a). Effects of Salinity, Organic Acids and Alkalinity in the Growth of Calcite Spherulites: Implications for Evaporitic Lacustrine Sedimentation. The Depositional Record, (December 2020), 1–22. https://doi.org/10.1002/dep2.136

Mercedes-Martín, R., Rogerson, M., Prior, T., Brasier, A., Reijmer, J., Billing, I., Matthews, A., Love, T., Lepley, S. and Pedley, M. (2021b). Towards a morphology diagram for terrestrial carbonates: evaluating the impact of carbonate supersaturation and alginic acid in calcite precipitate morphology. *Geochimica et Cosmochimica Acta*, In press.

Milodowski, A. E., Shaw, R. P., & Stewart, D. I. (2013). The Harpur Hill Site: its geology, evolutionary history and a catalogue of materials present. British Geological Survey Report. CR/13/104. Available from: https://rwm. nda. gov. uk/publication/harpur-hill-site-its-geology-evolutionary-history-and-a-catalogue-of-materials-present.

Pedley, M. (1992). Freshwater (phytoherm) reefs: the role of biofilms and their bearing on marine reef cementation. Sedimentary Geology, 79(1-4), 255-274.

Pedley, H.M. (1994) Prokaryote-microphyte biofilms and tufas: a sedimentological perspective. Kaupia-Darmstad. Beitr. Naturgesch., Heft 4, 45–60.

Pedley, M., Rogerson, M., & Middleton, R. (2009). Freshwater calcite precipitates from in vitro mesocosm flume experiments: a case for biomediation of tufas. Sedimentology, 56(2), 511-527.

Pentecost, A. (2005). Travertine. Springer Science & Business Media.

This article is protected by copyright. All rights reserved

Rainey, D. K., & Jones, B. (2009). Abiotic versus biotic controls on the development of the Fairmont Hot Springs carbonate deposit, British Columbia, Canada. Sedimentology, 56(6), 1832-1857.

Renforth, P., Manning, D. A. C., & Lopez-Capel, E. (2009). Carbonate precipitation in artificial soils as a sink for atmospheric carbon dioxide. Applied Geochemistry, 24(9), 1757-1764.

Riley, A. L., and Mayes, W. M. (2015). Long-term evolution of highly alkaline steel slag drainage waters. Environ. Monit. Assess. 187:463. doi: 10.1007/s10661-015-4693-1

Riley, A. L., MacDonald, J. M., Burke, I. T., Renforth, P., Jarvis, A. P., Hudson-Edwards, K. A., ... & Mayes, W. M. (2020). Legacy iron and steel wastes in the UK: Extent, resource potential, and management futures. Journal of Geochemical Exploration, 219, 106630.

Roadcap, G. S., Kelly, W. R., & Bethke, C. M. (2005). Geochemistry of extremely alkaline (pH> 12) ground water in slag-fill aquifers. Groundwater, 43(6), 806-816.

Rodriguez-Navarro, C., Jimenez-Lopez, C., Rodriguez-Navarro, A., Gonzalez-Muñoz, M. T., & Rodriguez-Gallego, M. (2007). Bacterially mediated mineralization of vaterite. Geochimica et Cosmochimica Acta, 71(5), 1197-1213.

Rogerson, M., Pedley, H. M., Wadhawan, J. D., & Middleton, R. (2008). New insights into biological influence on the geochemistry of freshwater carbonate deposits. Geochimica et Cosmochimica Acta, 72(20), 4976-4987.

Rogerson, M., Pedley, H. M., Kelham, A., & Wadhawan, J. D. (2014). Linking mineralisation process and sedimentary product in terrestrial carbonates using a solution thermodynamic approach. Earth Surface Dynamics, 2(1), 197-216.

Sant'Anna, L. G., Riccomini, C., Rodrigues-Francisco, B. H., Sial, A. N., Carvalho, M. D., & Moura, C. A. V. (2004). The Paleocene travertine system of the Itaboraí basin, Southeastern Brazil. Journal of South American Earth Sciences, 18(1), 11-25.

Saunders, P., Rogerson, M., Wadhawan, J. D., Greenway, G., & Pedley, H. M. (2014). Mg/Ca ratios in freshwater microbial carbonates: Thermodynamic, kinetic and vital effects. Geochimica et Cosmochimica Acta, 147, 107-118.

Shiraishi, Y., & Hirai, T. (2008). Selective organic transformations on titanium oxide-based photocatalysts. Journal of Photochemistry and Photobiology C: Photochemistry Reviews, 9(4), 157-170.

Accepted Article

This article is protected by copyright. All rights reserved

Solmaz, K. B., Ozcan, Y., Mercan Dogan, N., Bozkaya, O., & Ide, S. (2018). Characterization and production of extracellular polysaccharides (EPS) by Bacillus pseudomycoides U10. Environments, 5(6), 63.

Stewart, R., Xie, Q., Morneault, K., Sharp, C., Schwarzbauer, H., Taylor, T., ... & Paxson, V. (2007). Stream control transmission protocol.

Sutherland, I.W. (2001) Biofilm exopolysaccharides: a strong and sticky framework. Microbiology, 147, 3–9.

Takeno, N., 2005.Atlas of Eh-pH Diagrams. Geological Survey of Japan Open File Report.419 p. 102.

Taylor, P. M., & Chafetz, H. S. (2004). Floating rafts of calcite crystals in cave pools, central Texas, USA: crystal habit vs. saturation state. Journal of Sedimentary Research, 74(3), 328-341.

Teng, H. H., Dove, P. M., & De Yoreo, J. J. (2000). Kinetics of calcite growth: surface processes and relationships to macroscopic rate laws. Geochimica et Cosmochimica Acta, 64(13), 2255-2266.

Toffolo, M. B. (2020). Radiocarbon Dating of Anthropogenic Carbonates: What Is the Benchmark for Sample Selection?. Heritage, 3(4), 1416-1432.

U.S. Geological Survey [USGS] (2014). Alkalinity Calculator. Available at: http://or.water.usgs.gov/alk/ (accessed January, 2019).

Uysal, I. T., Zhao, J. X., Golding, S. D., Lawrence, M. G., Glikson, M., & Collerson, K. D. (2007). Sm–Nd dating and rare-earth element tracing of calcite: implications for fluid-flow events in the Bowen Basin, Australia. Chemical Geology, 238(1-2), 63-71.

Uysal, I. T., Feng, Y. X., Zhao, J. X., Isik, V., Nuriel, P., & Golding, S. D. (2009). Hydrothermal CO2 degassing in seismically active zones during the late Quaternary. Chemical Geology, 265(3-4), 442-454.

Uysal, I. T., Feng, Y. X., Zhao, J. X., Bolhar, R., Işik, V., Baublys, K. A., ... & Golding, S. D. (2011). Seismic cycles recorded in late Quaternary calcite veins: geochronological, geochemical and microstructural evidence. Earth and Planetary Science Letters, 303(1-2), 84-96.

Veysey II, J., & Goldenfeld, N. (2008). Watching rocks grow. Nature physics, 4(4), 310-313.

White, W. B. (2020). Rate processes: chemical kinetics and karst landform development (pp. 227-248). Routledge.

This article is protected by copyright. All rights reserved

Wolthers, M., Nehrke, G., Gustafsson, J. P., & Van Cappellen, P. (2012). Calcite growth kinetics: Modeling the effect of solution stoichiometry. Geochimica et Cosmochimica Acta, 77, 121-134.

Wright, V. P. (2012). Lacustrine carbonates in rift settings: the interaction of volcanic and microbial processes on carbonate deposition. Geological Society, London, Special Publications, 370(1), 39-47.

Zaihua, L., Svensson, U., Dreybrodt, W., Daoxian, Y., & Buhmann, D. (1995). Hydrodynamic control of inorganic calcite precipitation in Huanglong Ravine, China: Field measurements and theoretical prediction of deposition rates. Geochimica et Cosmochimica Acta, 59(15), 3087-3097.

Accepted Article

This article is protected by copyright. All rights reserved

Samples	BB1	Tunnel	BB10	BB13	BB14
pH	12.59	12.57	12.34	12.25	12.06
Temperature (°C)	16.9	16.2	17.6	17.4	19
Conductivity (µS)	8273	8290	4648	3410	2374
Major ions (ppm)					
Al^{+}	0.11	0.13	0.19	0.21	0.19
K^{+}	65.10	92.54	91.91	93.54	91.59
Na^{+}	62.58	35.97	50.77	51.70	51.47
Sr^{2+}	1.27	3.21	2.26	2.16	1.87
Ca^{2+}	744.49	697.52	328.54	225.86	155.94
Ba^{2+}	0.30	2.26	0.88	0.74	0.57
CO_3^{2-}	208.20	177.80	71.60	42.40	0.184
HCO_3^{-}	10.60	12.40	5.80	5.70	13.316
Total Alkalinity as $CaCO_3$ (ppm)	218.80	190.20	77.40	48.10	13.5
Calcite Saturation Index	2.71	2.65	2.21	1.96	0.43
Ionic strength ($mol.kgw^{-1}$)	$4.12.10^{-2}$	$3.84.10^{-2}$	$2.26.10^{-2}$	$1.74.10^{-2}$	$1.38.10^{-2}$
Activity					
Ca^{2+}	$5.72.10^{-3}$	$4.59.10^{-3}$	$5.59.10^{-3}$	$3.40.10^{-3}$	$2.10.10^{-3}$
CO_3^{2-}	$3.31.10^{-4}$	$2.39.10^{-4}$	$2.91.10^{-4}$	$1.73.10^{-4}$	$6.4.10^{-7}$
Calcite growth rate ($m.s^{-1}$)	$1.87.10^{-7}$	$1.22.10^{-7}$	$1.55.10^{-7}$	$6.38.10^{-8}$	$2.39.10^{-14}$

Table 1: Hydrochemistry dataset of the Brook Bottom samples including pH, temperature, major ion concentrations, total alkalinity, calcite saturation index, ionic strength, activity and calcite growth rate.

This article is protected by copyright. All rights reserved

Samples	C4	C5	C6	DB6	DB12	DB18
pH	9.06	10.06	11.51	10.72	10.35	10.50
Temperature (°C)	13.40	12.80	12.60	12.50	12.60	12.90
Conductivity (µS)	438.30	425.70	2165	452.40	436.50	427
Major ions ($mg.l^{-1}$)						
Ca^{2+}	11.18	11.97	161.22	14.46	11.80	12.50
Mg^{2+}	0.75	4.84	0.68	2.08	0.43	2.30
K^{+}	19.19	20.45	183.55	17.70	21.18	21.05
Na^{+}	24.43	27.36	49.88	24.81	27.53	28.40
OH^{-}	0.10	0.70	20.60	3.30	1.40	0.80
CO_3^{2-}	1.60	7.30	103.60	18.30	13.80	7.50
HCO_3^{-}	37.20	17.10	8.60	9.40	16.70	18.20
Total Alkalinity as $CaCO_3$ ($mg.l^{-1}$)	66	56	264	59	55	60
Calcite Saturation Index	0.04	0.25	2.30	0.96	0.67	0.23
Ionic strength ($mol.kgw^{-1}$)	$1.48.10^{-3}$	$1.95.10^{-3}$	$1.11.10^{-2}$	$2.01.10^{-3}$	$1.73.10^{-3}$	$3.50.10^{-3}$
Activity						
Ca^{2+}	$2.36.10^{-4}$	$2.39.10^{-3}$	$1.90.10^{-3}$	$2.56.10^{-4}$	$2.25.10^{-4}$	$2.25.10^{-3}$
CO_3^{2-}	$9.68.10^{-7}$	$2.79.10^{-5}$	$3.97.10^{-4}$	$1.36.10^{-4}$	$7.88.10^{-5}$	$2.65.10^{-5}$
Calcite growth rate ($m.s^{-1}$)	$3.43.10^{-11}$	$9.84.10^{-13}$	$4.39.10^{-10}$	$3.11.10^{-11}$	$1.30.10^{-11}$	$5.03.10^{-13}$

Table 2: Hydrochemistry dataset of the Consett samples including pH, temperature, major ion concentrations, total alkalinity, calcite saturation index, ionic strength, activity and calcite growth ratee from the research works of Mayes et al. (2008), Hull et al. (2014), Riley and Mayes (2015), Hobson et al. (2018), and Mayes et al. (2018)..

This article is protected by copyright. All rights reserved

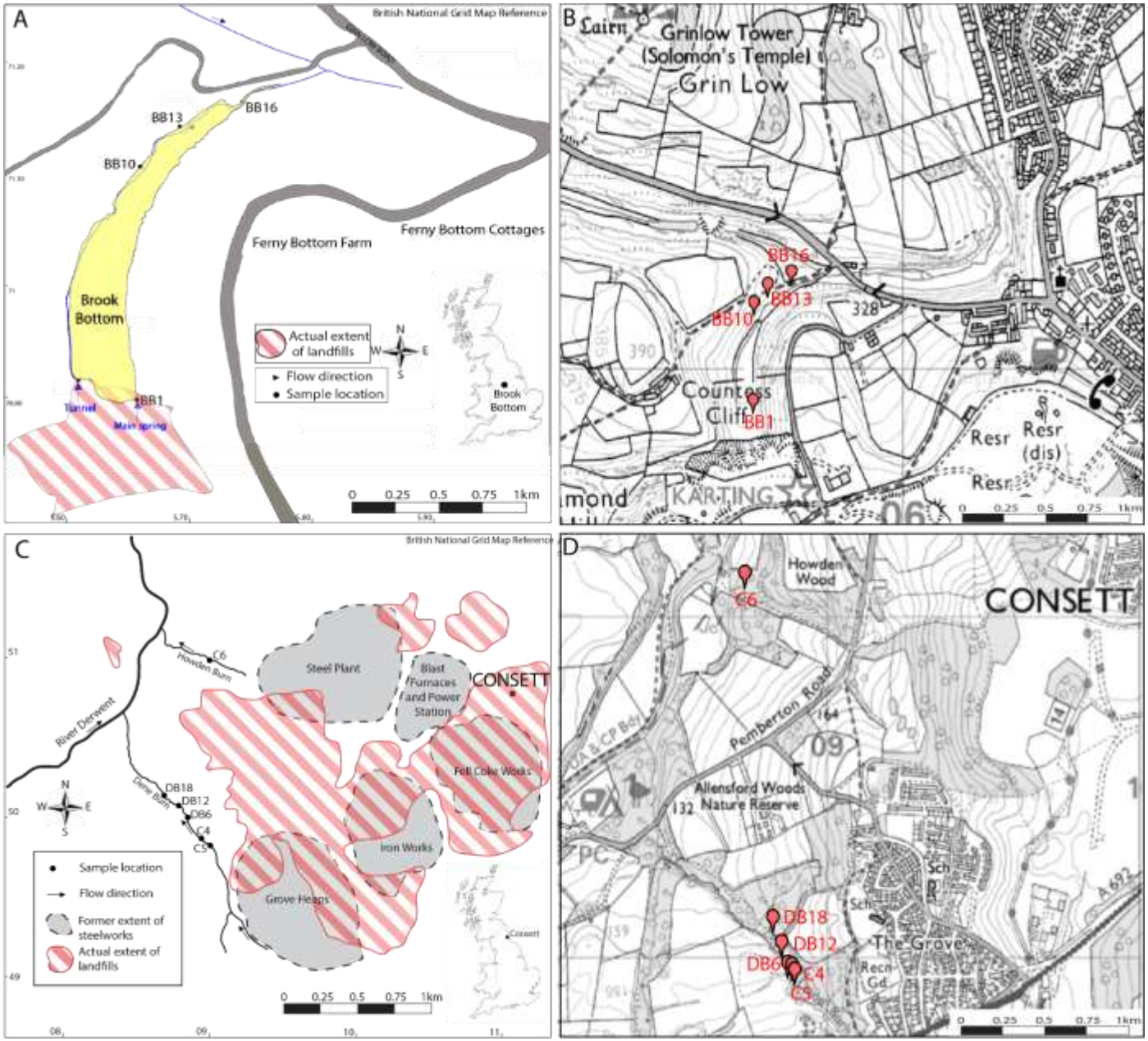

Figure 1: A- Location maps of the Brook Bottom (BB) samples (BB1, BB13, BB10 fresh, BB10 old deposit, BB16) where the yellow part represent the carbonate deposit; B- Topographic map with the Brook Bottom samples (BB1, BB13, BB10 fresh, BB10 old deposit, BB16) after Ordnance Survey map; C- Location map of the Consett (C) freshwater samples in Howden Burn (C6) and Dene Burn (DB) (C4, C5, DB6, DB12, DB18) after Historic OS maps; D- Topographic map with the Consett freshwater samples in Howden Burn (C6) and Dene Burn (C4, C5, DB6, DB12, DB18) after Ordnance Survey map.

This article is protected by copyright. All rights reserved

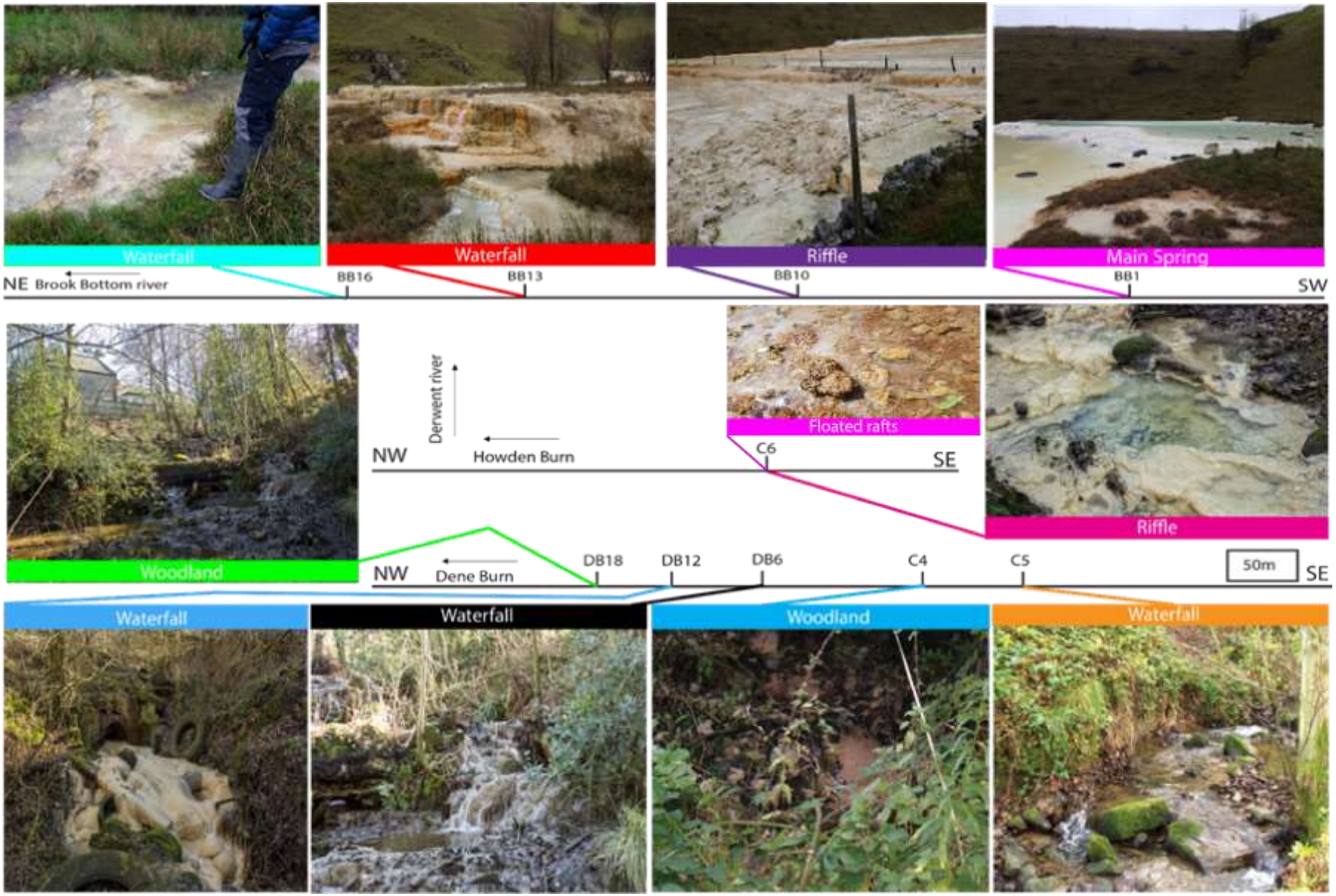

Figure 2: Environmental pictures of the downstream transects of Howden Burn, Dene Burn and Brook Bottom with the localization of the riffle, waterfall, and woodland.

This article is protected by copyright. All rights reserved

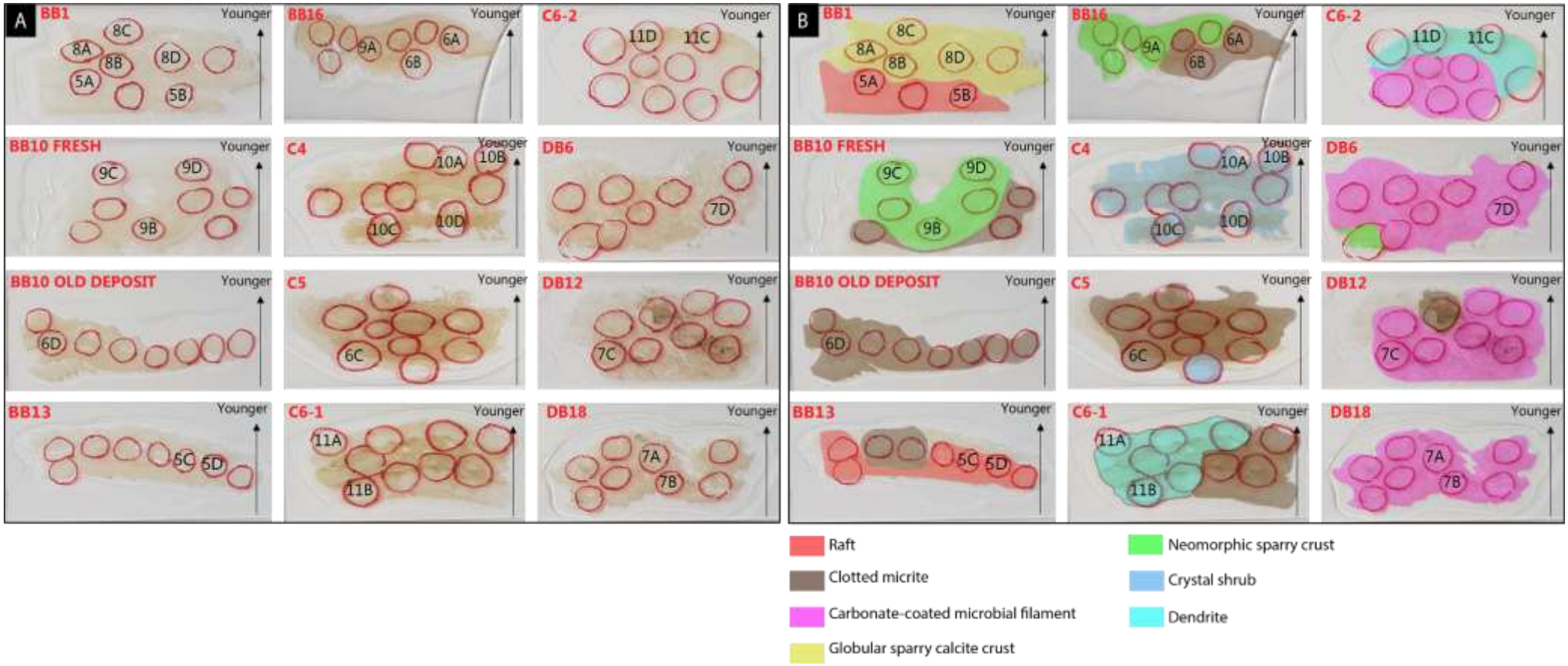

Figure 3: (A) Original thin sections from the Brook Bottom (BB) (BB1, BB13, BB10 fresh, BB10 old deposit, BB16) and Consett (C) freshwater samples in Howden Burn (C6) and Dene Burn (DB) (C4, C5, DB6, DB12, DB18) with the locations of the optical microscope images. The locations are respectively designated by the number of the figure from this manuscript followed by the letter corresponding to the subsection in the figure. (B) Interpreted thin-sections with the colours representing the different microfacies. The locations of the optical microscope images are respectively designated by the number of the figure from this manuscript followed by the letter corresponding to the subsection in the figure.

This article is protected by copyright. All rights reserved

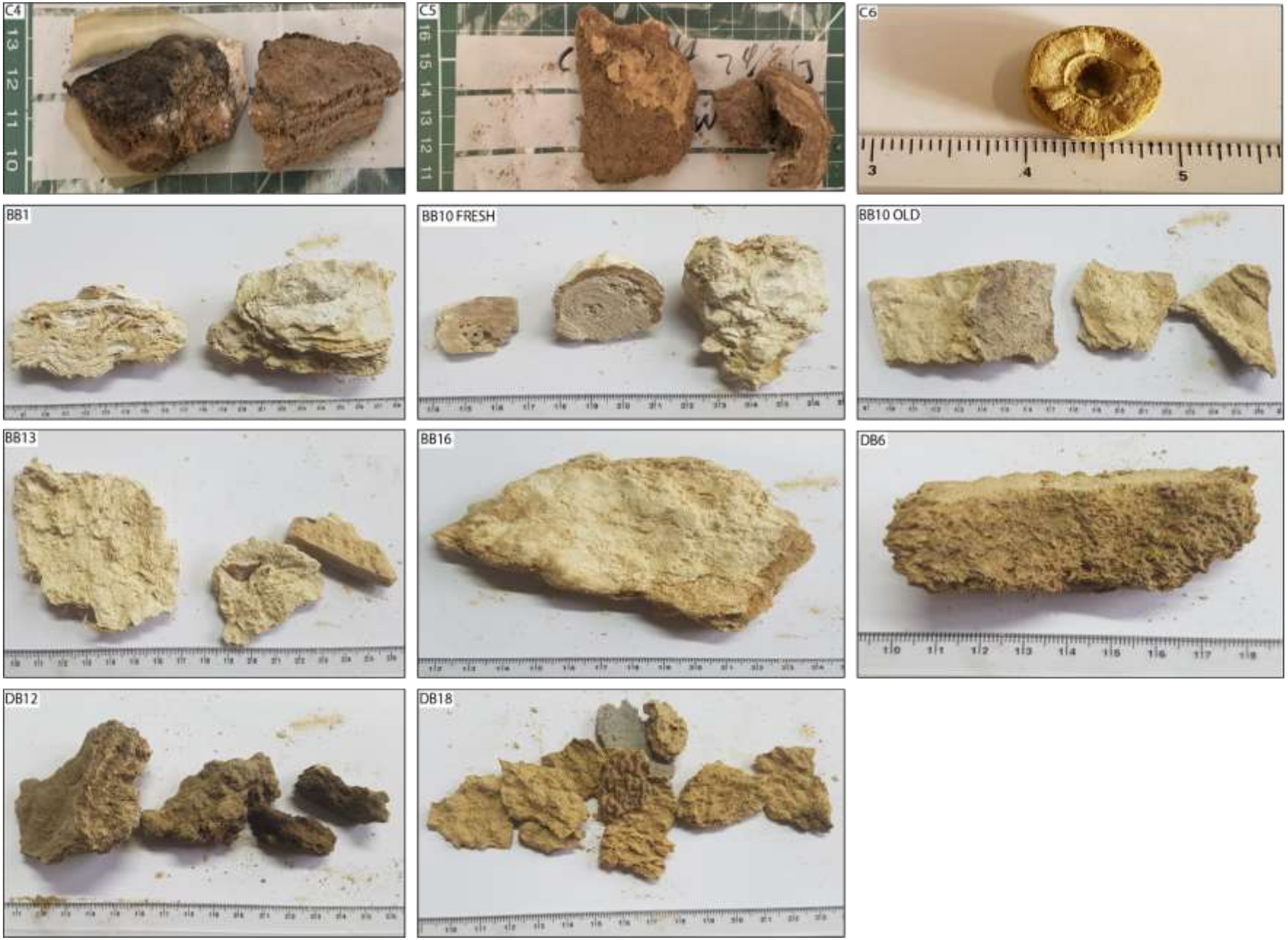

Figure 4: Macroscopic images of the Brook Bottom (BB) (BB1, BB13, BB10 fresh, BB10 old deposit, BB16) and Consett (C) freshwater samples in Howden Burn (C6) and Dene Burn (DB) (C4, C5, DB6, DB12, DB18).

This article is protected by copyright. All rights reserved

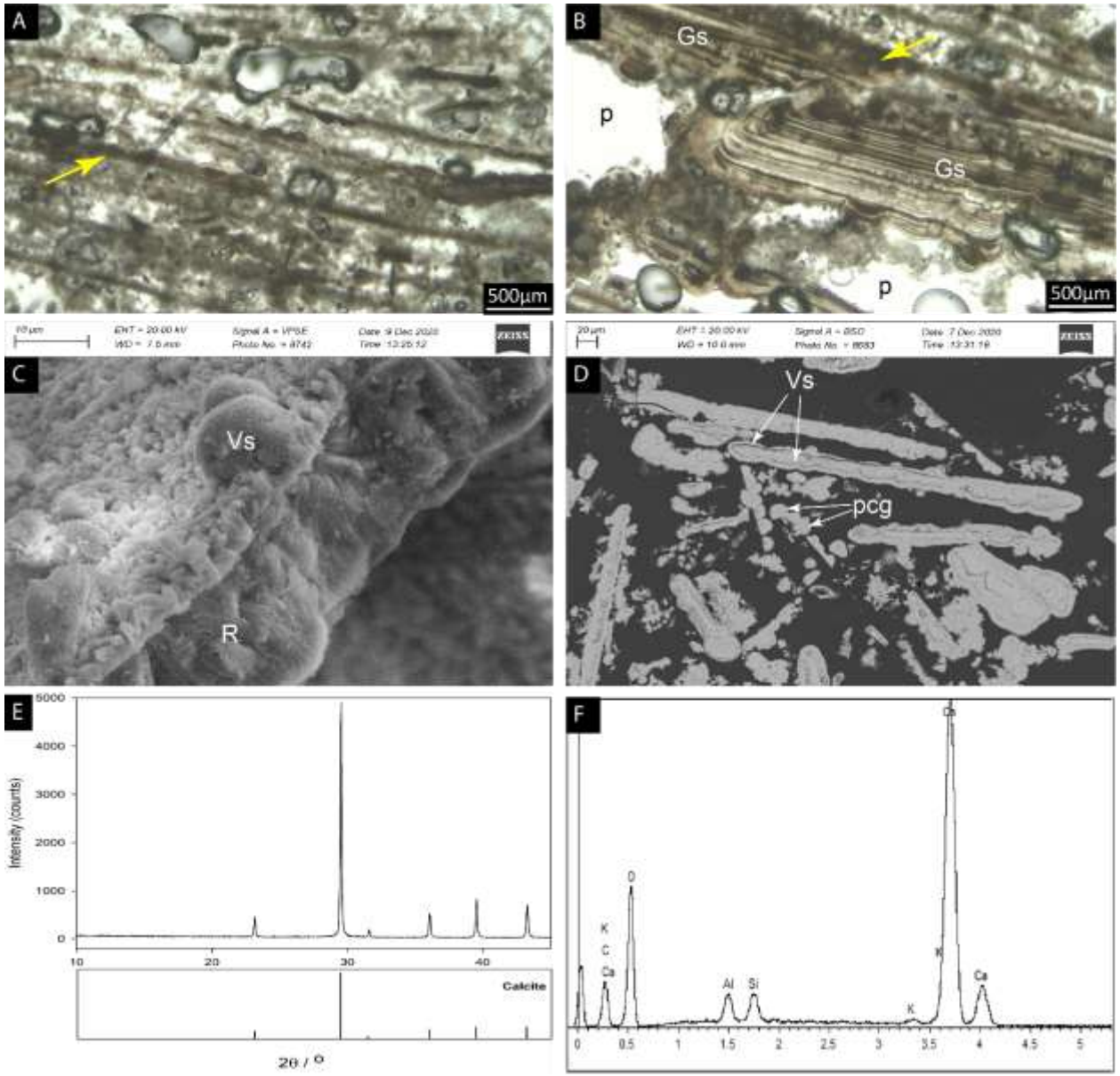

Figure 5: Coated vegetative remains and carbonate raft (microfacies 1). A) Assemblage of brown coloured, flat and elongated vegetated remains (arrow) coated by calcite thin films. B) Some flat remains (arrow) are covered in globular sparry calcite crusts (Gs); interparticle porosity (p) is very abundant. C) SEM photomicrograph of carbonate rafts (R) covered by multiple arcuate vault structures (Vs) constituted by cloudy, brown-coloured sparry calcite. D) BSE-SEM image of poorly sorted carbonate rafts covered by vault structures (VS). Some polycrystalline calcite globular aggregates (pcg) can grow laterally to form elongated occurrences. E- F) XRD pattern and EDX spot analysis, respectively, indicating a calcite mineralogy.

This article is protected by copyright. All rights reserved

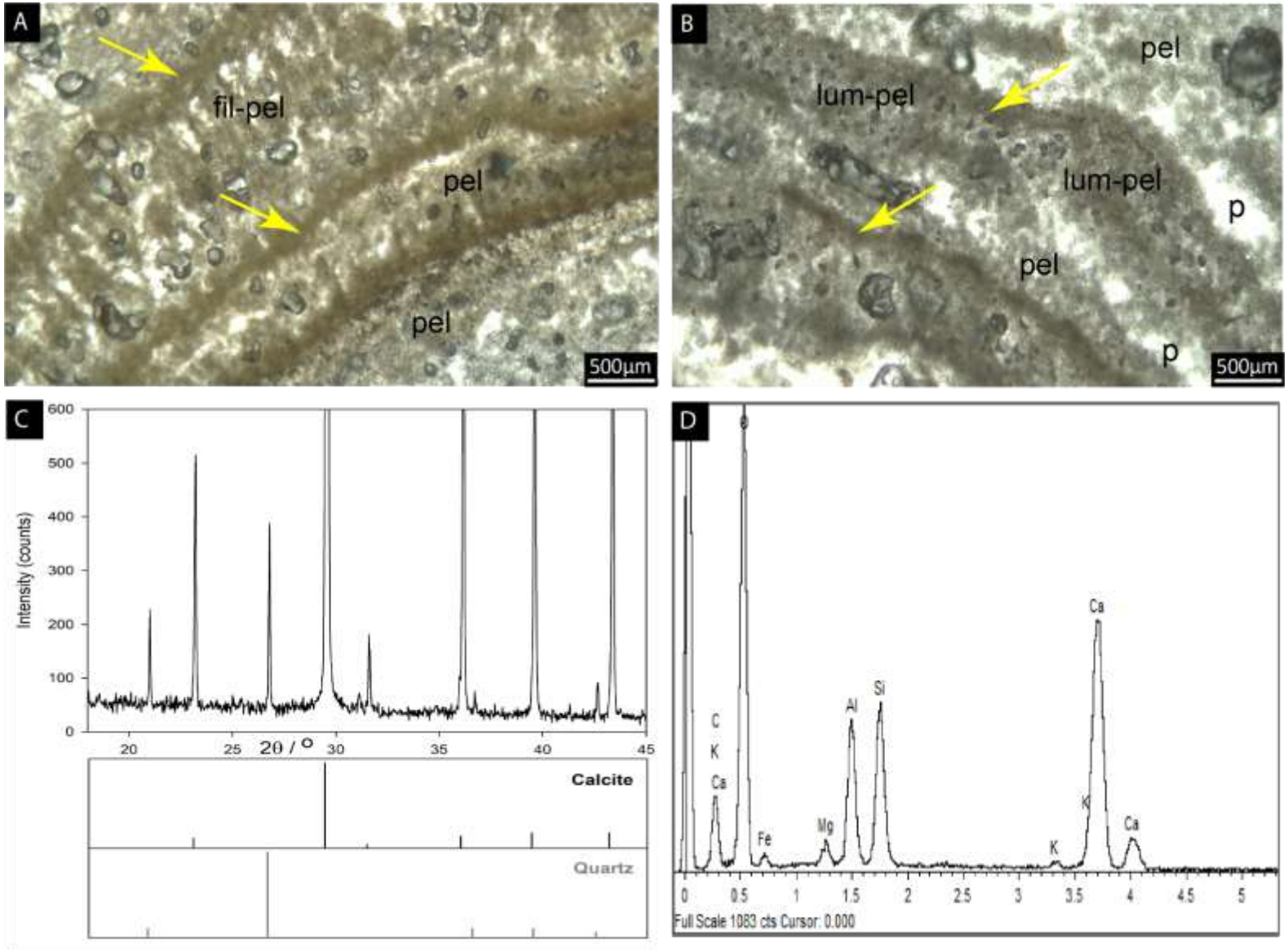

Figure 6: Micro-peloidal and clotted micritic (microfacies 2). A–B) Patchy micropeloidal micritic textures (pel) alternate with laminated textures (arrows). Filamentous clotted structures can be seen perpendicular to laminae (fil-pel). In some cases, lumpy micropeloidal masses (lum-pel) develop in association to laminated textures. Abundant inter-crystalline porosity (p) is observed in this microfacies. C-D) XRD pattern and EDX spot analysis, respectively, indicating that calcite and quartz are present.

This article is protected by copyright. All rights reserved

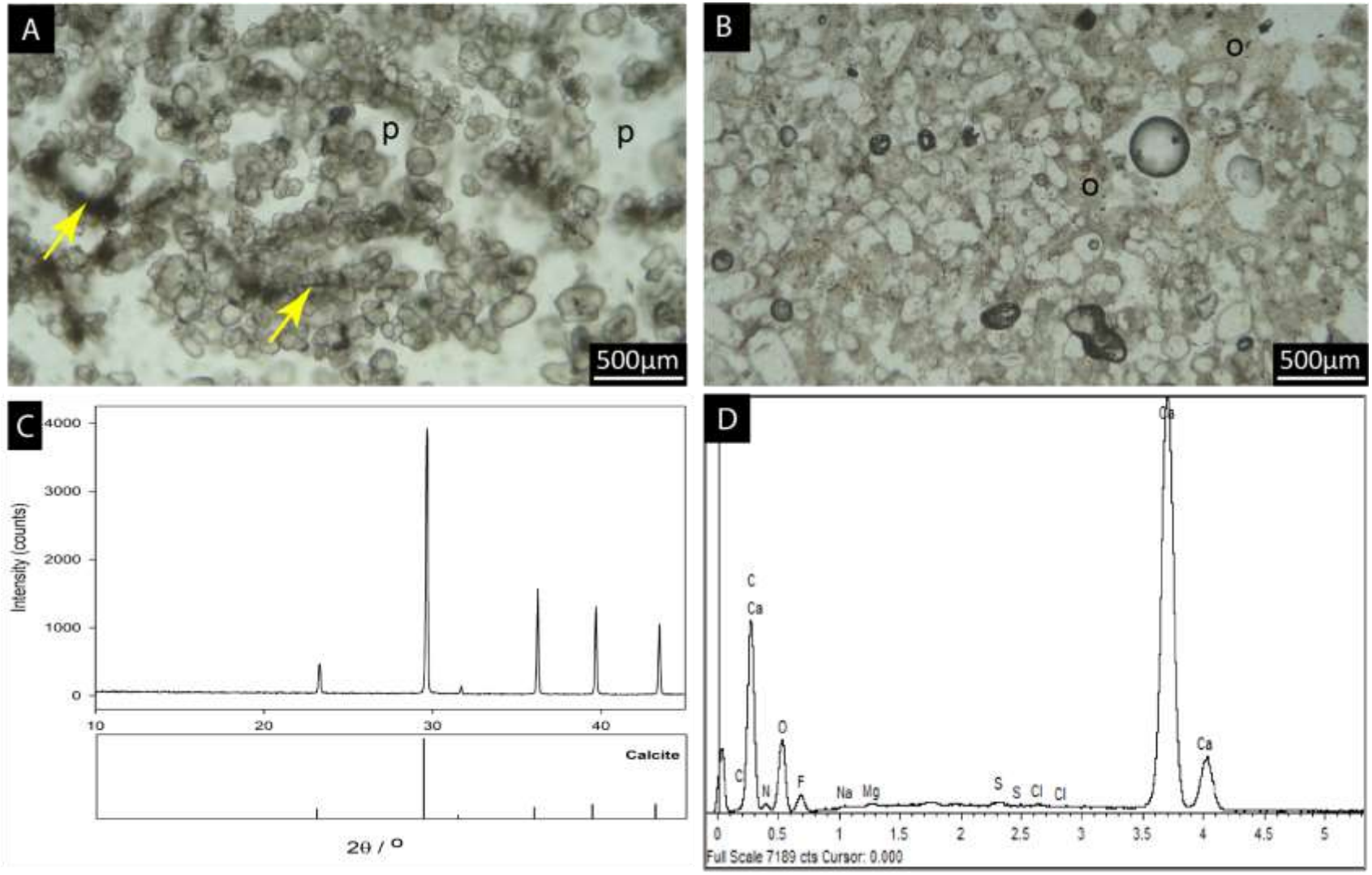

Figure 7: Carbonate-coated microbial filament (microfacies 3) A) Double terminating calcite crystal morphologies agglutinated around organic-rich filamentous structures (arrows) forming crystal lumps. High intercrystalline porosity (p) is recognised between filaments. B) Double terminating calcite crystal can be detached from microbial filaments forming intraclastic accumulations embedded in organic-rich matrices (o). C - D) XRD pattern and EDX spot analysis, respectively, indicating that calcite is the predominant mineralogy.

This article is protected by copyright. All rights reserved

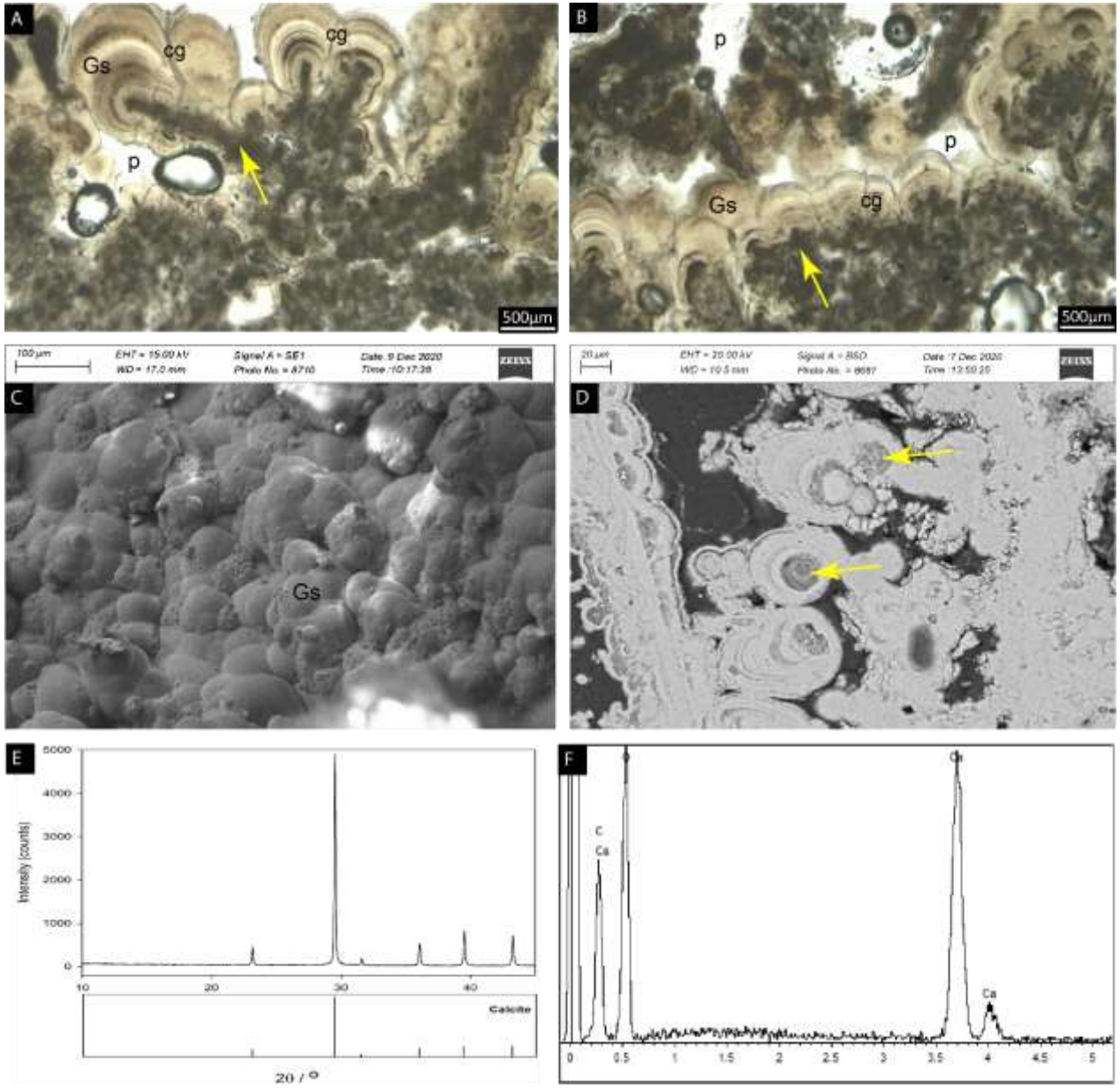

Figure 8: Globular sparry calcite crust (microfacies 4). A–B) Thick isopachous calcite fans with globular arrangements (Gs) growing on top of clotted peloidal templates (arrows). Fans are constituted by thin darker laminae and thick lighter laminae extending laterally. Competitive growth defines sharp boundaries between fans (cg). This microfacies display a high intercrystalline porosity (p). C) SEM image showing the external smooth curved surfaces of the fans (Gs). D) BSE-SEM image displaying sparry crusts growing on top of organic substrates (arrows). Note thin concentric, darker laminae within fans. E-F) XRD pattern and EDX spot analysis, respectively, indicating that calcite is the predominant mineralogy.

This article is protected by copyright. All rights reserved

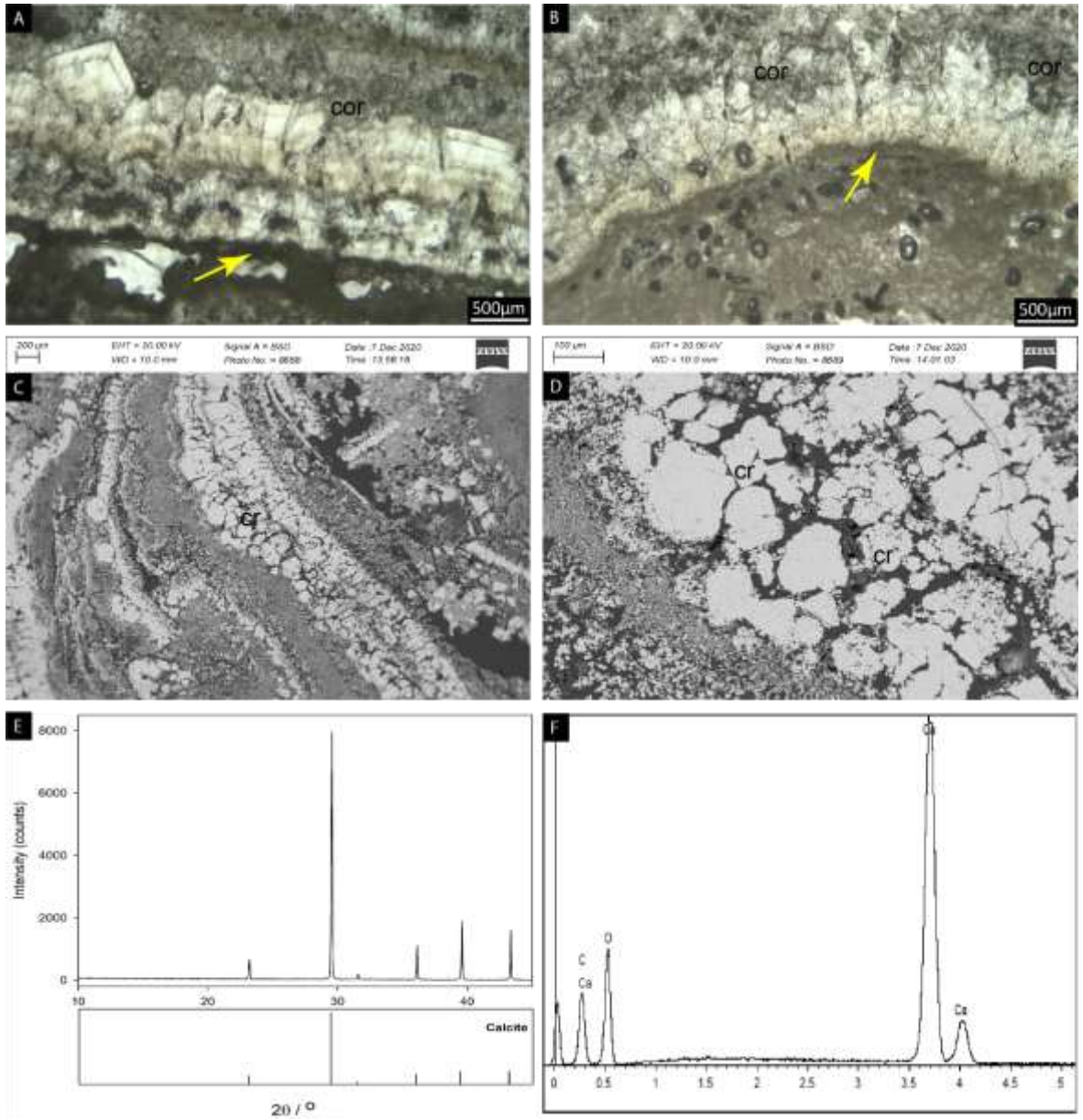

Figure 9: Neomorphic sparry crust (microfacies 5). A–B) Neomorphic sparry crusts growing on top of organic-rich substrates (arrows). Corroded areas (cor) through irregular surfaces on the external part of the crusts are common. C-D) BSE-SEM images showing cracking of the crusts where fissures (cr) reach different depths showing no apparent reworking. E-F) XRD pattern and EDX spot analysis, respectively, indicating that calcite is the predominant mineralogy.

This article is protected by copyright. All rights reserved

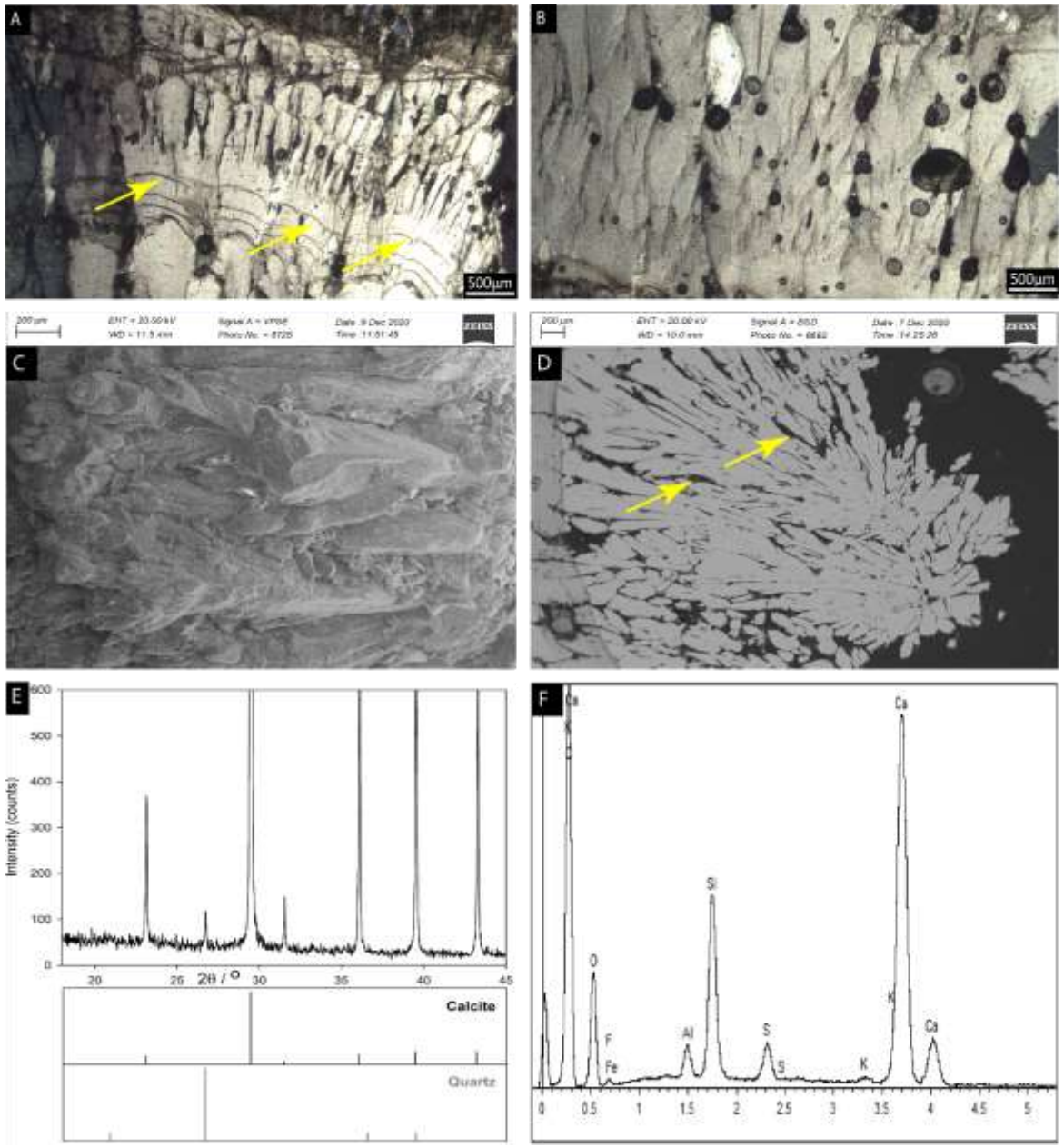

Figure 10: Crystal shrub (microfacies 6). A–B) Light grey-white botryoidal like crystal fans 1–3 mm in height and stacked each other as inverted cones growing on top of discontinuous horizons (arrows). C-D) BSE-SEM images showing bladed crystal aggregates developing incipient intercrystalline microporosity (arrows). E-F) XRD pattern and EDX spot analysis, respectively, indicating that calcite and quartz are present.

This article is protected by copyright. All rights reserved

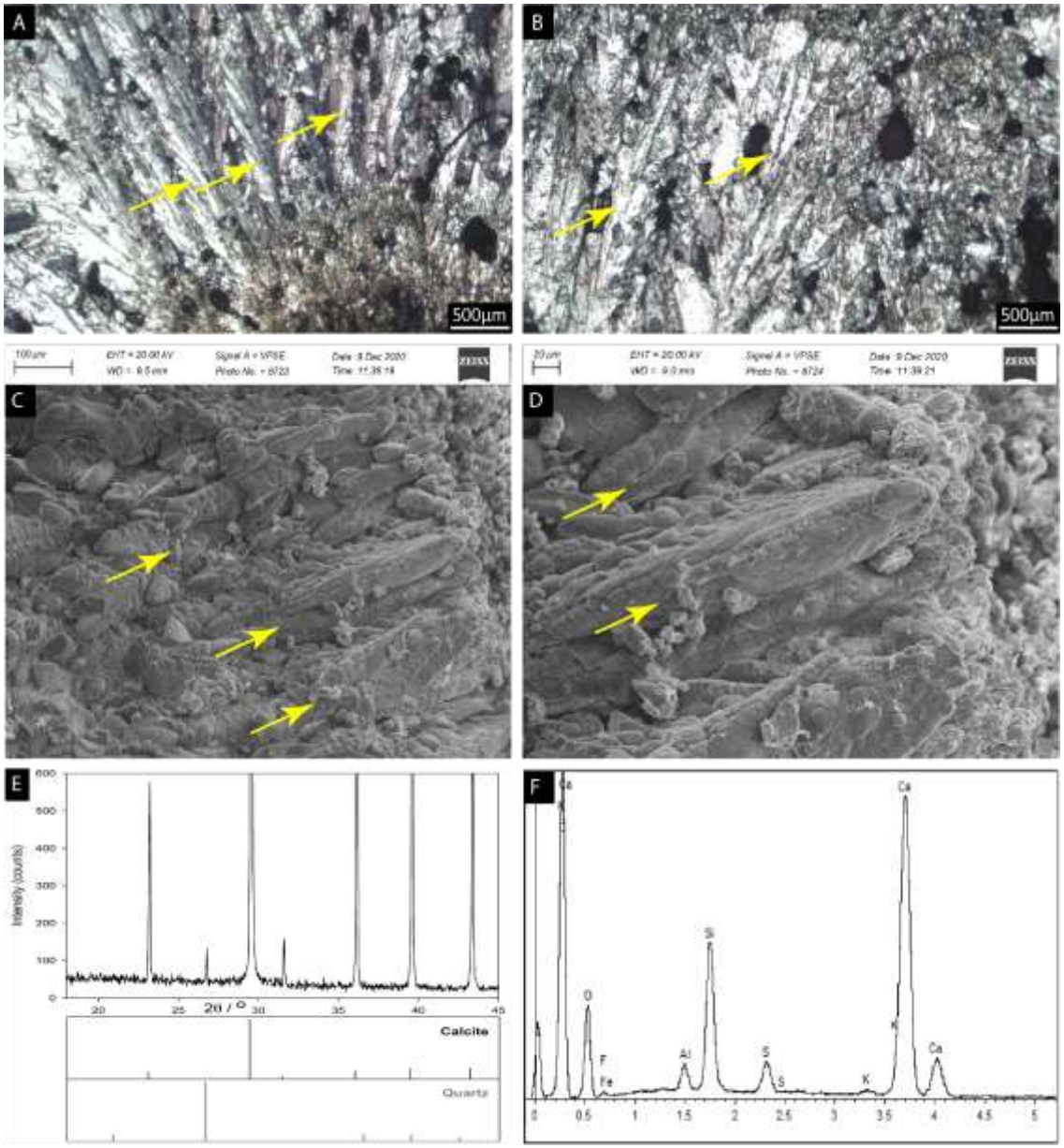

Figure 11: Dendrite carbonates (microfacies 7). A–B) light grey calcite polycrystals showing multiple levels of branching (arrows). C-D) BSE-SEM images showing that each branch consists of numerous thin (up to 0.2 mm thick), plate-like calcite crystals that are stacked in echelon (arrows). E-F) XRD pattern and EDX spot analysis, respectively, indicating that calcite and quartz are present.

This article is protected by copyright. All rights reserved

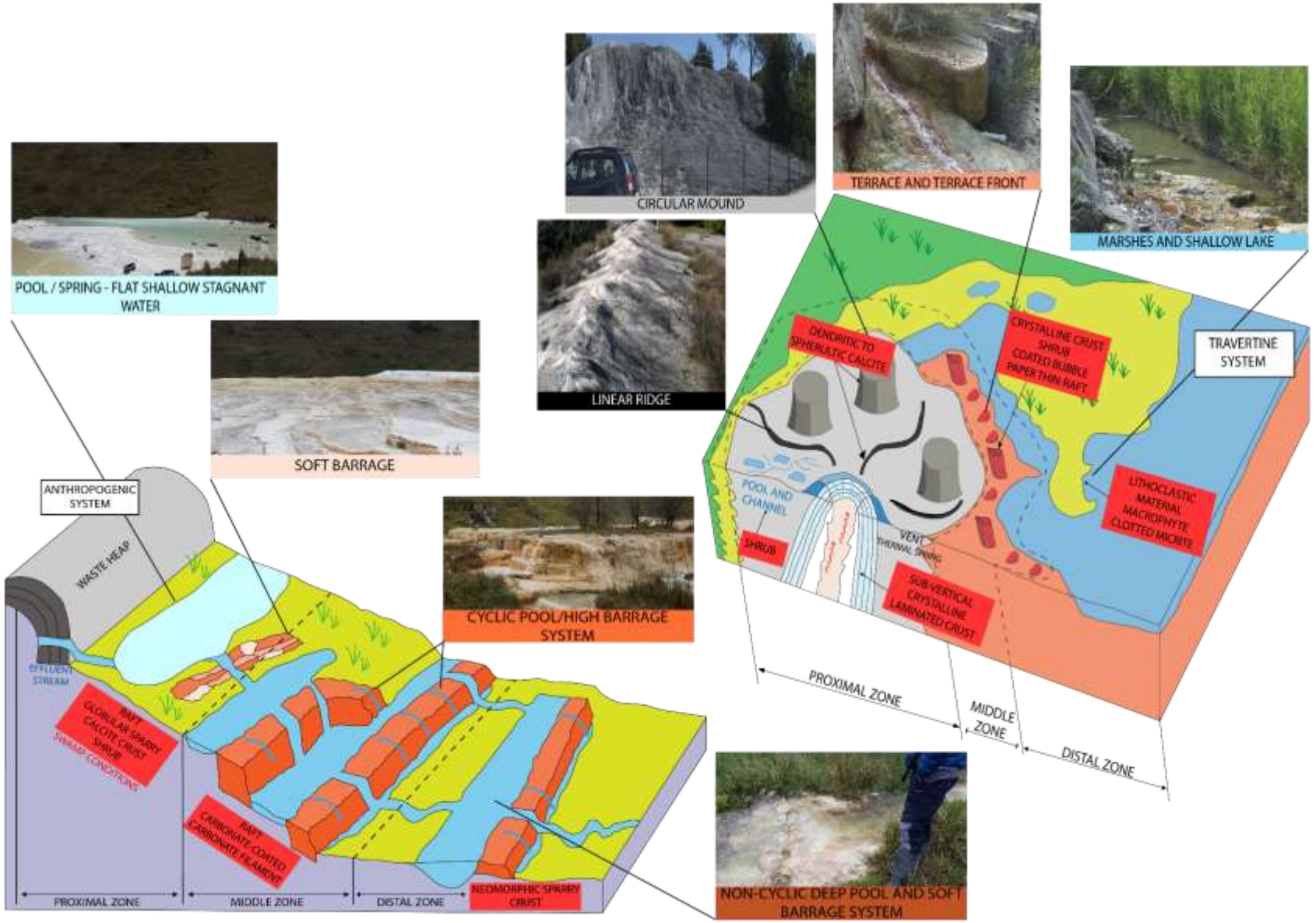

Figure 12: Comparative depositional model between anthropogenic carbonate and travertine systems after Capezuolli et al. (2014) and Mancini et al. (2019).

This article is protected by copyright. All rights reserved

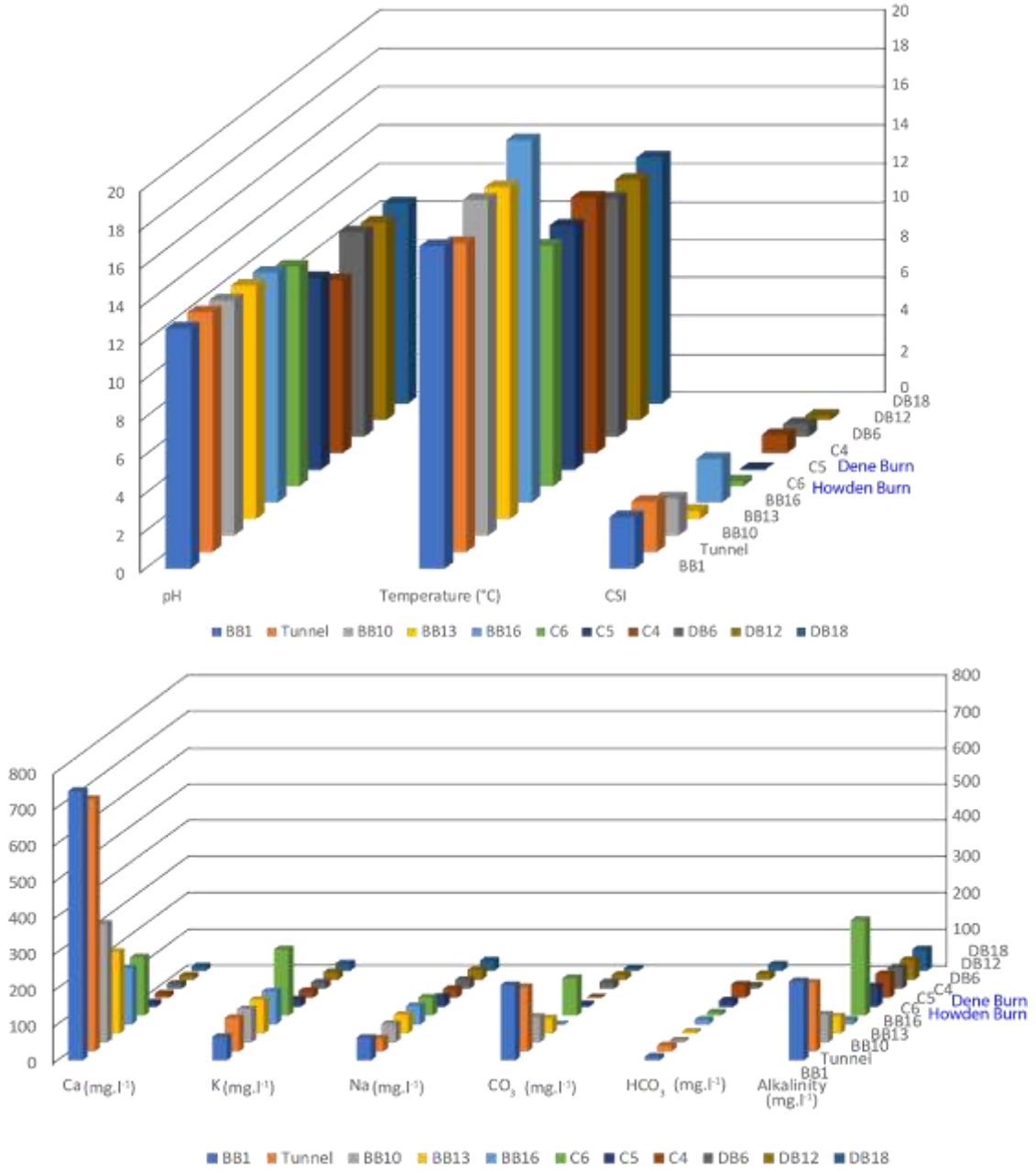

Figure 13: Charts showing the pH, temperature and Calcite Saturation Index (CSI) and the major ions and total carbonate alkalinity for the Brook Bottom and Consett samples.

This article is protected by copyright. All rights reserved

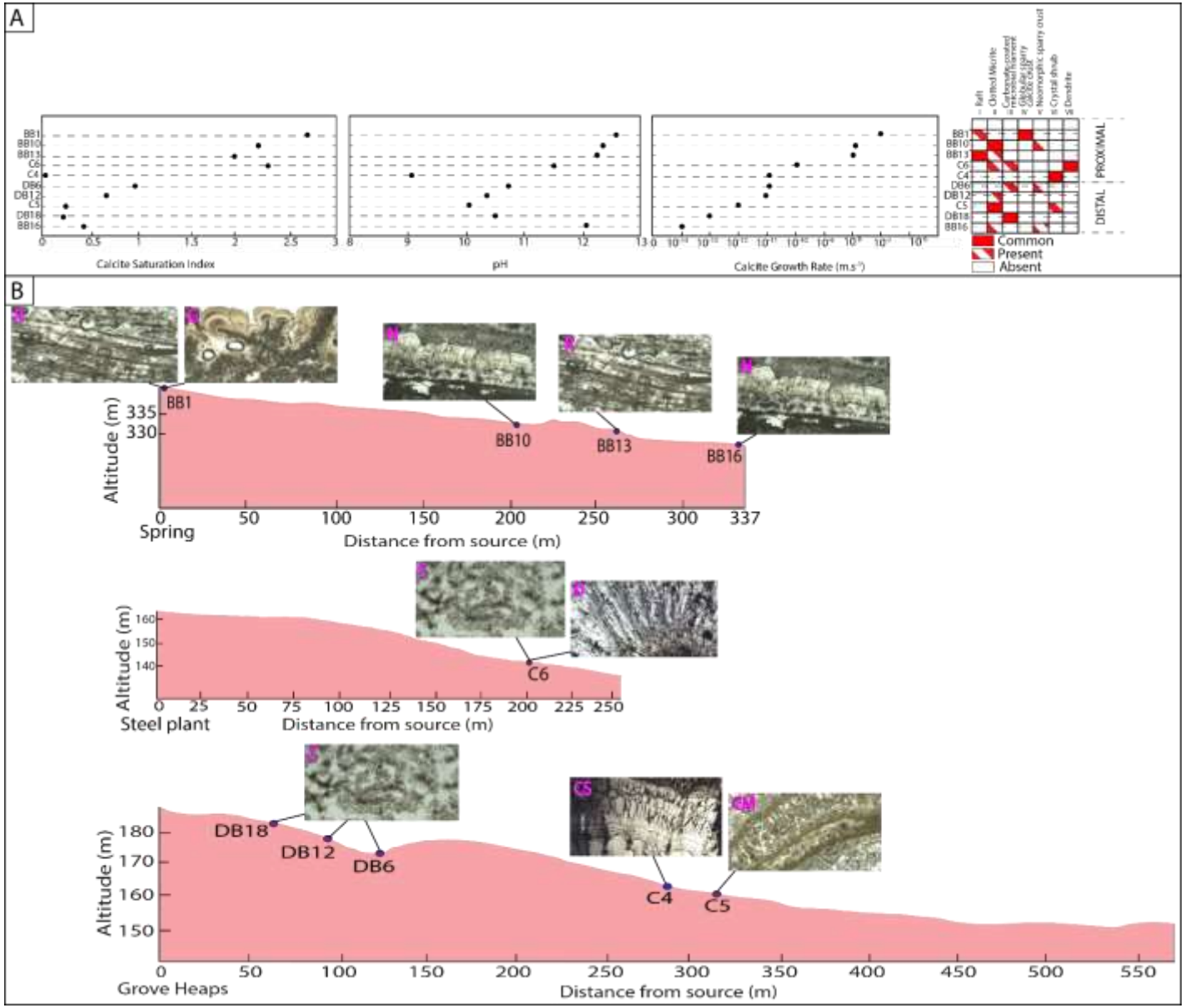

Figure 14 A) Diagram showing the Calcite Saturation Index (CSI), pH, calcite growth rate (R) versus distribution of microfacies according to the sample locations of Brook Bottom (BB) BB1, BB13, BB10 fresh, BB10 old deposit, BB16 and Consett (C) freshwater samples in Howden Burn (C6) and Dene Burn (DB) (C4, C5, DB6, DB12, DB18); B) shows the depositional model summarising the lateral changes of the dominant microfacies: Coated vegetative remains and carbonate raft (R), Micro-peloidal and clotted micritic (CM), Carbonate-coated microbial filament (C), Globular sparry calcite crust (G), Neomorphic sparry crust (N), Crystal shrub (CS) and Dendrite (D).

This article is protected by copyright. All rights reserved